UNIVERSITY OF TARTU
Faculty of Science and Technology
Institute of Chemistry

Amina Aliyeva

# Synthesis of High-Performance FeCo-N-C Oxygen Electrocatalysts via Zn-TAL MOF Metamorphosis

Master's Thesis (30 ECTS)

Curriculum Materials Science and Technology

Supervisors:
Nadežda Kongi, Ph.D
Gulnara Yusibova, M.Sc

Tartu 2024

## Synthesis of High-Performance FeCo-N-C Oxygen Electrocatalysts via Zn-TAL MOF Metamorphosis

**Abstract:**

The urgency to mitigate climate change has catalyzed a global shift towards renewable energy, highlighting the importance of efficient energy solutions like fuel cells and metal-air batteries. The oxygen reduction reaction and oxygen evolution reaction are central to their performance, which requires active catalysts due to their slow kinetics. In this master thesis, highly active oxygen electrocatalysts were successfully synthesized through the carbonization of Fe/Co-Zn-coordinated TAL materials without the need for precious metals. The physicochemical properties were investigated using XRD, $N_2$-physisorption, STEM, and XPS, and the electrochemical behavoiur was screened by cyclic voltammetry and rotating disc electrode techniques. This research offers significant insights into the design of practical, high-performance catalysts for FCs and MABs.

**Keywords:** Bifunctional Electrocatalyst, Electrocatalysis, Metal-Organic Materials, Oxygen Reduction Reaction (ORR), Oxygen Evolution Reaction (OER).

**CERCS:** P395 Organometallic chemistry, P400 Physical chemistry, P401 Electrochemistry

## Tõhusate FeCo-N-C hapniku elektrokatalüsaatorite süntees Zn-TAL MOFi metamorfoosi abil

**Lühikokkuvõte:**

Kliimamuutuste leevendamise kiireloomulisus on katalüüsinud ülemaailmset üleminekut taastuvenergiale, rõhutades tõhusate energialahenduste, nagu kütuseelemendid ja metall-õhk aukud, tähtsust. Hapniku redutseerimisreaktsioon ja hapniku eraldumise reaktsioon on nende toimimise kesksel kohal, mis nõuavad nende aeglase kineetika tõttu aktiivseid katalüsaatoreid. Selles magistritöös sünteesiti edukalt kõrge aktiivsusega hapniku elektrokatalüsaatoreid Fe/Co-Zn-koordineeritud TAL materjalide karboniseerimise teel, ilma et oleks vaja kasutada väärismetalle. Füüsikalis-keemilisi omadusi uuriti XRD, $N_2$-physisorption, STEM ja XPS abil ning materjalide elektrokatalüütilist aktiivsust uutiti tsüklilise voltammeetria ning pöörleva ketaselektroodi meetodiga. See uurimus pakub märkimisväärset teavet FC-de ja MAB-de praktiliste suure jõudlusega katalüsaatorite kavandamise kohta.

**Võtmesõnad:** Bifunktsionaalsed elektrokatalüsaatorid, elektrokatalüüs, metall-orgaanilised materjalid, hapniku redutseerumisreaktsioon (ORR), hapniku eraldumise reaktsioon (OER).

**CERCS:** P395 Orgaaniline metallkeemia, P400 Füüsikaline keemia, P401 Elektrokeemia

# TABLE OF CONTENTS

## ABBREVIATIONS

**AEMs** -anion exchange membranes

**AEMFCs** - anion exchange membrane fuel cells

**BET** - Brunauer–Emmett–Teller

**CV** - cyclic voltammetry

**DFT** - density functional theory

**EIS** - electrochemical impedance spectroscopy

**FCs** - fuel cells

**HAADF** - high-angle annular dark field

**HER** - hydrogen evolution reaction

**$IrO_2$** - iridium dioxide

**I2M** - intermolecular O–O coupling

**K-L** - Koutecký–Levich

**LIBs** - lithium-ion batteries

**LSV** - linear sweep voltammetry

**M-N-C** - metal nitrogen doped carbon

**M−$N_x$** - metals coordinated to nitrogen

**MABs** - metal-air batteries

**MP-AES** - microwave plasma-atomic emission spectroscopy

**N-C** - nitrogen-doped carbon

**NMR** - nuclear magnetic resonance

**NPs** - nanoparticles

**OER** - oxygen evolution reaction

**ORR** - oxygen reduction reaction

**PEMFCs** - proton exchange membrane fuel cells

**PGM** - platinum-group metals

**PXRD** - powder x-ray diffraction

**$RuO_2$** - ruthenium dioxide

**RDE** - rotating disk electrode

**SHE** - standard hydrogen electrode

**SOFCs** - solid-oxide fuel cells

**STEM** - scanning transmission electron microscopy

**TEM** - transmission electron microscopy

**TM** - transition-metal

**TMO** - transition-metal oxides

**WNA** - water nucleophilic attack

**XAS** - X-ray absorption spectroscopy

**XPS** - x-ray photoelectron spectroscopy

**ZABs** - zinc-air batteries

**ZIF** - zeolitic imidazolate framework

**Zn-MOFs** - zinc-based metal-organic frameworks

***$E_{onset}$*** - onset potential

***$E^0$*** - standard reduction potential

**$\Delta E$** - potential difference

**$\Delta G^0$** - free energy difference

$i_d$ - diffusion current

$i_k$ - kinetic current

$v$ - potential scan rate

$\eta$ - overpotential

$\omega$ - electrode rotation speed

# INTRODUCTION

The global shift towards renewable energy, driven by the urgency to address climate change, emphasizes the growing importance of alternative energy solutions.[1,2] Among these, fuel cells (FCs) and metal-air batteries (MABs) have emerged as viable options for efficient energy conversion and storage with minimal environmental effects.[3,4] Within the domain of electrochemistry, the oxygen reduction reaction (ORR) and oxygen evolution reaction (OER) assume paramount importance, particularly in clean energy systems like FCs and MABs. ORR, however, presents intrinsic issues because of its slow kinetics.[5] To address this, active cathode catalysts are essential to accelerate the reaction to practical levels for fuel cell operation.[6–8] Platinum-group metals (PGM) and their alloys are known for their superior ORR/OER performance as catalyst materials. However, their high cost, limited availability, and sensitivity to deterioration are substantial inhibitors to wider commercialization.[9] Thus, the search for cost-effective and long-lasting platinum (Pt) - free catalyst materials remains a vital area of research and development in promoting their general use and integration into the global energy infrastructure.[10]

Exploring alternatives such as transition metal oxides, nanoparticles, and nanocomposites reveals significant limitations, including sluggish kinetics, insufficient active sites, and stability issues.[11] In response, transition metal and nitrogen-doped carbon (M-N-C) catalysts emerge as a promising alternative, offering high catalytic activity, stability, and cost-effectiveness.[12] This study focuses on developing novel M-N-C bifunctional electrocatalysts, including Fe-, Co-, and FeCo-N-C, with a particular emphasis on bimetallic FeCo-N-C, designed to exhibit superior activity and stability in both ORR and OER.

Similarly to noble metal-based catalysts iron and cobalt offer high oxygen electroactivity and stability in alkaline electrolytes at lower costs compared to Pt.[13] They promote the ORR via a direct 4-electron pathway and are feasible alternatives to Pt in alkaline fuel cell cathodes.[14]

In this work, the morphology of the prepared catalyst was investigated using several physical characterization techniques ($N_2$-physisorption, PXRD, STEM, XPS, MP-AES), and the obtained results were thoroughly correlated with the electrochemical performance, evaluated by cyclic voltammetry (CV) and rotating disk electrode (RDE) techniques. The objectives of this work were to provide valuable insights into the rational design of Fe-, Co, and FeCo-N-C catalysts for ORR and OER.

# 1 LITERATURE REVIEW

## 1.1 Fuel Cells

Fuel cells (FC) are poised to be instrumental in advancing a sustainable energy future by offering eco-friendly, efficient, and dependable power generation options for numerous uses. These electrochemical devices convert chemical energy into electrical energy by catalyzing a reaction between a fuel source and an oxidizing agent.[15] There are various types of fuel cells, such as alkaline anion-exchange membrane fuel cells (AEMFCs) and solid alkaline fuel cells (SOFCs) or proton-exchange membrane fuel cells (PEMFCs).

AEMFCs represent a promising advancement in fuel cell technology, leveraging anion exchange membranes (AEMs) to facilitate the electrochemical reactions necessary for power generation. Unlike traditional PEMFCs, which use proton exchange membranes to conduct protons, AEMFCs use AEMs to transport hydroxide ions ($OH^-$) from the cathode to the anode.[16] The core components in AEMFCs are the anion exchange membrane, anode, cathode, and the fuel, typically hydrogen. At the anode, hydrogen gas ($H_2$) is oxidized, releasing electrons and producing water and hydroxide ions (Fig, 1).[17] The overall reaction at the anode can be described as $2H_2 + 4OH^- \rightarrow 4H_2O + 4e^-$.[17] These electrons travel through an external circuit, generating electrical power. At the cathode, oxygen ($O_2$) from the air combines with water and the incoming electrons to produce hydroxide ions, which then migrate back to the anode through the anion exchange membrane: $O_2 + 2H_2O + 4e^- \rightarrow 4OH^-$.[17] The cell reaction is $2H_2 + O_2 \rightarrow 2H_2O$ + electrical energy + heat.

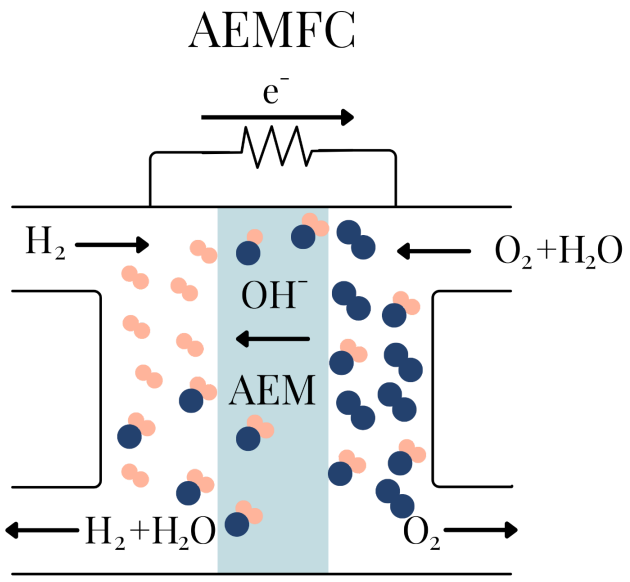


**Figure 1.** Diagram illustrating the operational process of AEMFC.

One of the significant advantages of AEMFCs is their operation in an alkaline environment.[17] This environment reduces the corrosion of cell components, allowing the use of less expensive, non-precious metal catalysts such as iron, nickel, and cobalt.[18] This factor can significantly lower the overall cost of the fuel cell. The alkaline medium in AEMFCs also improves the kinetics of both the oxygen reduction reaction at the cathode and the hydrogen oxidation reaction at the anode. Faster reaction kinetics lead to higher fuel cell efficiency and performance, making AEMFCs highly efficient power sources.[18] AEMFCs exhibit reduced fuel crossover compared to PEMFCs.[17] In PEMFCs, the proton exchange membrane can allow some hydrogen or other fuel to pass through, reducing efficiency. The structure of AEMs minimizes this issue, thereby enhancing the cell's overall fuel utilization and efficiency.[17]

Despite their advantages, AEMFCs face several challenges. One of the primary issues is the lower ionic conductivity of anion exchange membranes compared to proton exchange membranes.[18] Work is ongoing to develop new materials and membrane designs to enhance the conductivity and overall performance of AEMFCs.[19,20] Another challenge is the durability and stability of the membranes in high-pH conditions.[18] The membranes must maintain their mechanical and chemical integrity over long periods, even in the presence of high concentrations of hydroxide ions. Innovative approaches in membrane chemistry and engineering are being explored to address these issues.[18]

AEMFCs hold significant potential for various applications, including portable power systems, stationary power generation, and transportation. Their ability to use non-precious metal catalysts and operate efficiently in an alkaline environment makes them a cost-effective alternative to other fuel cell technologies.[18,21,22] In the future, ongoing research and development are expected to overcome the current challenges, further enhancing the performance and durability of AEMFCs.[19,20] As these advancements continue, AEMFCs could play a crucial role in the transition to sustainable and renewable energy sources, contributing to a cleaner and more energy-efficient future.[19,20]

Finally, fuel cells offer an environmentally conscious approach to electricity generation, utilizing an electrochemical process that yields solely water and heat, in contrast to conventional power generation methods notorious for emitting pollutants and greenhouse gases.[23]

## 1.2 Metal-Air Batteries

While lithium-ion batteries (LIBs) have been instrumental in various applications, their limitations in safety, resource availability, and energy density have prompted exploration into alternative technologies. Metal-air batteries (MABs), particularly zinc-air batteries (ZABs), are gaining attention as promising alternatives to traditional LIBs due to their numerous advantages, including higher theoretical energy density, abundance of zinc resources, and inherent safety features like non-flammability.[24–26] With theoretical energy densities reaching up to 1086/1350 W h $kg^{-1}$ (including/excluding oxygen), MABs outshine LIBs, which typically offer a mere 350 W h $kg^{-1}$.[27–30] ZABs offer the potential for longer-lasting power sources across a wide range of applications, from portable electronics to grid-scale energy storage systems.[31,32]

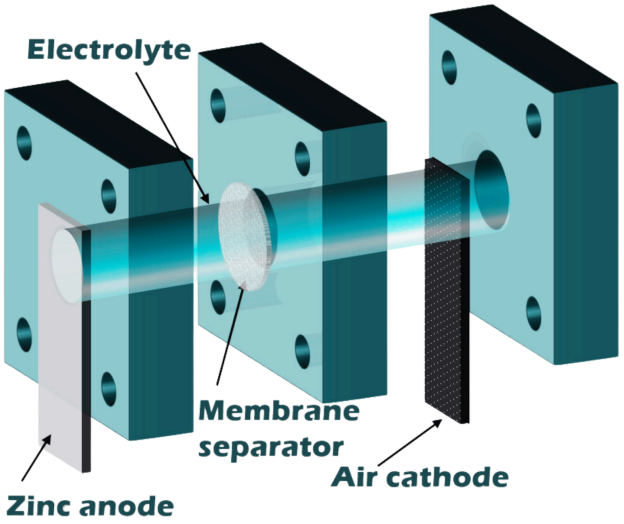


**Figure 2.** General schematic of Zn-air battery.

Typically, a secondary ZAB includes an electrolyte, air cathode, zinc anode, membrane separator and current collectors (Fig. 2). The electrolyte conducts ions between electrodes, affecting ZAB rechargeability, power density, lifespan, and voltage. Ideally, the electrolyte should have high ionic conductivity, low electron conductivity, minimal self-discharge, non-corrosiveness, and stability in various conditions, while being environmentally friendly and cost-effective. Alkaline aqueous electrolytes are common for their low viscosity, high conductivity, affordability, and wide availability. However, they can suffer from electrolyte carbonation, ZnO precipitation, water loss, and anode corrosion or dendrite formation, impacting ZAB performance. Our research group is developing methodologies to enhance ionic strength, promote uniform zinc deposition, and modify cell reaction mechanisms by incorporating additives.[33]

To commercialize ZAB technology, an affordable and abundant air electrode catalyst is essential, replacing currently available Pt-group metal-based bifunctional electrocatalysts.[34–37] The air electrode in ZABs requires a bifunctional catalyst to catalyze both the ORR and the OER. ORR occurs during discharge via two routes in an alkaline environment: direct $4e^-$ reduction or $2e^-$ reduction, followed by a further $2e^-$ reduction. Conversely, during charging, the OER must be catalyzed at the air electrode to ensure high round-trip efficiency.[34,38]

Currently, PGM-based bifunctional electrocatalysts are the benchmark for these reactions due to their excellent catalytic properties. However, these materials are expensive and scarce, which poses a significant barrier to the widespread adoption of ZABs. Therefore, the development of cost-effective, abundant, and efficient alternative catalysts is essential for the commercialization of ZAB technology. Ongoing research is focused on exploring various materials, such as transition metal oxides, carbon-based materials, and metal-nitrogen-doped carbons, which could serve as viable replacements for PGMs in the air electrode.[39–41]

In summary, while ZABs offer numerous advantages over LIBs, including higher energy density, safety, and the use of abundant materials, the development of affordable and efficient air electrode catalysts is crucial for their commercial viability. Overcoming this challenge will pave the way for ZABs to become a key player in the next generation of energy storage technologies.

## 1.3 ORR

The ORR is a multielectron process with numerous basic stages and reaction intermediates. The ORR kinetics is usually extremely sluggish. A cathode ORR catalyst is required to accelerate the ORR kinetics to a level that is viable for use in fuel cells.

The ORR in acidic solutions can proceed via two primary pathways: a two-electron transfer leading to the formation of $H_2O_2/HO_2^-$, or a four-electron transfer resulting in the production of $H_2O/OH^-$. The pathway chosen depends on how $O_2$ adsorbs onto the catalyst's active sites and the binding strength involved.[42–44] In the dissociative mechanism, $O_2$ adsorbs onto two neighbouring active sites, creating MOH intermediates that are eventually reduced to $H_2O$. Alternatively, the associative mechanism involves the end-on adsorption of $O_2$, forming MOOH intermediates, which can then be further reduced to either $H_2O$ or $H_2O_2$.[45]

The standard reduction potential ($E^0$) of $O_2$ to $OH^-$, is 0.401 V versus the standard hydrogen electrode (SHE) for the direct four-electron pathway. Typically, the target reaction is the

4-electron pathway depicted in Equation 1.[46] The two-electron pathways include the combination of Equations 2 and 3, where $H_2O_2$ is produced as an intermediate, and Equations 2 and 4, which lead to an incomplete reduction.[46]

$$O_2 + 4H^+ + 4e^- \rightleftharpoons 2H_2O \qquad E^0 = 1.229 \text{ V vs. SHE} \qquad (1)$$

$$O_2 + 2H^+ + 2e^- \rightleftharpoons H_2O_2 \qquad E^0 = 0.655 \text{ V vs. SHE} \qquad (2)$$

$$H_2O_2 + 2H^+ + 2e^- \rightleftharpoons 2H_2O \qquad E^0 = 1.776 \text{ V vs. SHE} \qquad (3)$$

$$2H_2O_2 \rightleftharpoons 2H_2O + O_2 \qquad (4)$$

Optimizing catalytic activity in the four-electron reduction pathway to $H_2O$ presents a challenge due to the presence of several intermediates with strongly correlated binding energies.[47,48] Strategies have been developed to regulate the electronic structure and customize active sites based on scaling relations to address this.[43,49,50] For example, theoretical calculations suggest an overpotential of approximately 0.3–0.4 V for the most efficient ORR catalysts like Pt, which aligns well with experimental data. These insights guide the design of advanced catalysts for improved ORR performance.[42,49,51]

## 1.4 OER

The OER is a vital electrochemical process for various energy storage and conversion technologies, including water electrolysis, metal-air batteries, and fuel cells. This process, which occurs near the anode of an electrochemical cell, converts electrical energy into chemical energy by splitting water into oxygen and protons, making it crucial for renewable energy generation.

The OER is a complex four-electron transfer process that requires greater applied potentials than the thermodynamic equilibrium potential (1.23 V vs. RHE) for oxidizing $H_2O/OH^-$ to $O_2$.[52,53] In general, the reaction occurs via two pathways: water nucleophilic attack (WNA) or the interaction of intermolecular O–O coupling (I2M).[54,55] In the WNA pathway (Fig. 3), $H_2O$ dissociates into $OH^-$, which then adsorbs at the catalyst's active site, forming a metal-oxo intermediate. This intermediate is nucleophilically attacked by another water molecule, leading to the formation of MOOH and subsequent release of $O_2$. Alternatively, the I2M

pathway (Fig. 3) involves the interaction between two metal-oxo species, resulting in the formation of $O_2$. The specific conditions of the reaction, such as whether it occurs in an acidic or alkaline environment, significantly impact the initial reactants and the intermediate stages of the process.[56]

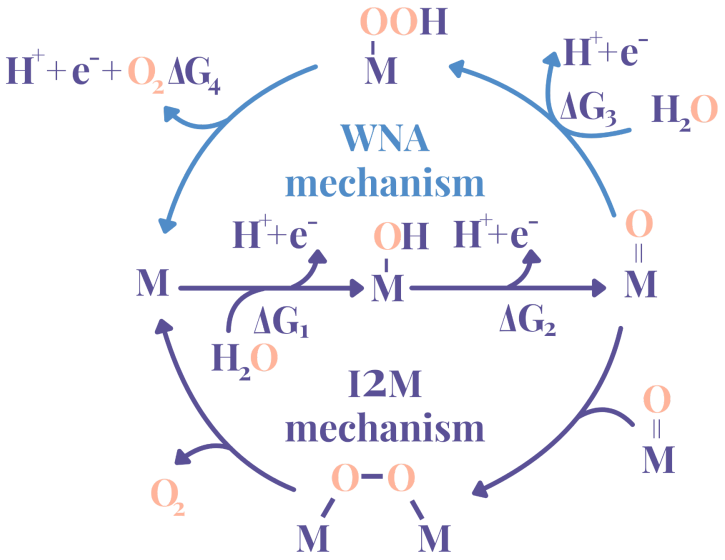


**Figure 3.** Schematic of OER process via WNA and I2M mechanisms.

The performance of OER catalysts is frequently hindered by the formation of multiple intermediates, making it essential to regulate the binding energies of these intermediates at the active sites. According to the Sabatier principle, an ideal OER catalyst should achieve optimal bond strength to promote adsorption and desorption processes.[57] Density functional theory (DFT) studies have developed scaling relations for binding energy differences, aiding in the rational design of catalysts by using volcano plots that plot the overpotential (ηOER) against the difference in free energies (ΔGO – ΔGOH).[58,59] However, during catalysis, catalysts often experience structural changes, which complicates the identification of the actual active centers.[60–63]

## 1.5 Electrocatalysts for ORR and OER

Electrocatalysts are pivotal components in a wide array of electrochemical devices, with Pt-based catalysts like Pt/C playing indispensable roles in AEMFCs due to their exceptional ORR performance.[64] To further enhance their stability and activity, innovative strategies such as surface modifications with oxides and the utilization of modified carbon supports like nitrogen-doped carbon (N-C) have been explored. These advancements hold promise for

significantly improving the durability and efficiency of Pt-based catalysts, essential for practical applications in fuel cells and beyond.[65–68]

In contrast, while Pt-based catalysts excel in ORR, ruthenium dioxide ($RuO_2$) and iridium dioxide ($IrO_2$) are known for their prowess in OER in acidic environments, a critical process for applications like water electrolysis.[69] However, their practical use is impeded by their high cost, limited availability, and susceptibility to oxidation.[70] Consequently, extensive research efforts are underway to develop high-performance PGM-free electrocatalysts, aiming to address these challenges and advance next-generation energy storage and conversion technologies.[71]

Metal oxide nanoparticles (NPs) are considered highly effective catalysts for OER. Their unique properties, such as high surface area and tunable electronic structures, make them suitable for OER applications. Sun et al. developed $Co_9S_8$ nanocages using ZIF-67 templates, discovering that the unique hollow structure of these NPs – significantly improves OER performance.[72] The $Co_9S_8$ shells prevent the aggregation of active centers, enhancing electrocatalytic activity and durability. Xiao et al. produced cobalt sulfides/nitrogen and sulfur dual-doped hollow carbon sphere (CoSx/N, S-HCS) electrocatalyst using a straightforward method involving ZIF-67.[73] Their work demonstrated that the homogeneous dispersion of cobalt sulfide nanoparticles in the carbon matrix leads to high OER activity due to improved electron transfer and stability under reaction conditions.[74]

Numerous studies have also highlighted the advantageous role of transition metal NPs encaged within a few layers of N-doped carbon in enhancing bifunctional ORR/OER activity. Multimetallic catalysts, doped with two or three transition metals such as Fe, Co, and Ni, exhibit superior electrocatalytic properties compared to single metal catalysts.[74–77] These catalysts feature diverse active sites that play crucial roles in facilitating efficient OER electrocatalysis, although the exact synergistic effects of these multimetallic sites remain ambiguous.[78,79] Furthermore, achieving a microstructure conducive to efficient mass transfer is imperative for attaining optimal electrocatalytic performance and facilitating the release of $O_2$ bubbles..[80]

Advancements in catalyst design aim to optimize performance under specific conditions by unraveling the intricate kinetics involved in OER.[69] Factors such as the electronic structure of the catalyst and the pH of the electrolyte significantly influence reaction mechanisms and efficiency, underscoring the importance of tailoring catalysts to these conditions.[69] Ongoing

research in electrocatalyst development is crucial for enhancing energy storage and conversion technologies.

Transition-metal (TM) and nitrogen co-doped nanocarbon materials present themselves as promising alternatives for both ORR and OER. These catalysts utilize transition metals coordinated to nitrogen ($M-N_x$) sites for ORR and transition metal oxides (TMO) for OER.[36,81] Recent reports suggest that both $M-N_x$ and TMO sites can significantly enhance the efficiency of both reactions, offering potential solutions to the limitations posed by traditional PGM-based catalysts.[36,81–83]

To conclude, while Pt-based catalysts have long dominated electrochemical applications due to their outstanding ORR performance, recent advancements have opened avenues for alternatives. Single-atom site catalysts, particularly transition metal nitrogen doped carbon catalysts (M-N-C), have emerged as promising contenders. M-N-C catalysts offer abundant active sites for both ORR and OER catalysis and improved stability, presenting viable options to replace PGMs.[84]

## 1.6 M-N-C Catalysts

M-N-C catalysts represent promising alternatives to PGMs in catalyzing ORR and OER due to their high activity and durability. These materials are crucial for advancing fuel cell technology, particularly in the development of AEMFCs. Constructed from abundant and cost-effective elements, M-N-C materials promise to achieve electrocatalytic efficiency exceeding that of precious metal-based alternatives under diverse circumstances. Among these alternatives, iron triad metals (Fe, Co, and Ni) stand out for their affordability, wide availability, and proven effectiveness in fuel cells and metal-air batteries.[74]

The nitrogen species in M-N-C materials (pyridinic, graphitic, pyrrolic, and oxidized nitrogen) promote the ORR, though the primary contributor to ORR activity remains debated.

In M-N-C catalysts, single-atom sites are particularly noteworthy for their exceptional catalytic activity in ORR. Among various configurations, $M-N_x$ sites are considered the most active. The $M-N_x$ sites refer to configurations where metal is coordinated with nitrogen atoms within a carbon matrix. The high ORR activity of these sites is attributed to the unique electronic properties imparted by the metal-nitrogen coordination, significantly influencing the catalytic performance.[85]

Compared to Pt-based catalysts, M-N-C systems offer a cost-effective and environmentally friendly alternative. M-N-C catalysts generally show superior performance due to their optimal adsorption energies for ORR intermediates, which align closely with the Sabatier principle.[86]

Pyridinic nitrogen moieties are highly regarded as active sites for the ORR, enhancing catalytic activity when integrated into a carbon matrix. Research shows that pyridinic nitrogen improves ORR performance by facilitating electron transfer and optimizing oxygen molecule adsorption. These moieties increase electron density around active sites, aiding oxygen adsorption and reduction, which are crucial for ORR. Pyridinic nitrogen's electron-donating properties improve interaction with oxygen intermediates, boosting catalytic efficiency. Additionally, the strong covalent bonds between nitrogen and carbon contribute to the catalyst's structural stability and lifespan.[87] In the research on nitrogen-doped carbon spheres, Wu et al. stated that pyridinic-N sites significantly enhance ORR activity by improving electron density and creating more active sites.[88] Another study by García-Rosado et al. on cobalt-pyridinic N moieties on reduced graphene oxide found that pyridinic nitrogen enhances interaction with oxygen intermediates, leading to higher catalytic activity in alkaline media.[87] This suggests that the combination of Fe-N-C and Co-N-C catalysts with pyridinic nitrogen moieties provides a promising pathway for developing efficient, stable, and cost-effective electrocatalysts for ORR applications.

The efficacy of bifunctional M-N-C catalysts for both ORR and the OER relies on the synthesis methods employed, which significantly influence their structure and performance. M-N-Cs are often synthesized via pyrolysis of metal-containing precursors, such as metal salts or organic compounds, in the presence of nitrogen sources and carbonaceous materials.[89–91]

## 1.7 MOF-Derived M-N-C Catalysts

MOFs have emerged as versatile precursors for creating M-N-C materials.[92,93] Recent studies by Salunkhe et al. revealed that zeolitic imidazolate framework-67 (ZIF-67) derived carbon can form graphitized carbon walls with a high specific surface area of 350 $m^2\ g^{-1}$ after being treated in a nitrogen atmosphere at 800 °C and subsequently subjected to HF treatment to remove metal ions.[94] Other examples of MOF-derived carbon materials include research by Xia et al., who produced N-doped carbon nanotubes through direct thermal treatment of

ZIF-67 particles in an $Ar/H_2$ atmosphere at 700 °C.[95] Additionally, Ye et al. generated 3D porous carbons by pyrolyzing an oxygen-rich zinc-containing MOF.[96] Zhang et al. managed to create highly graphitized nitrogen-doped porous carbon with an impressive specific surface area of 932 $m^2 g^{-1}$ using ZIF-8, treated under a nitrogen atmosphere at 1000 °C for 10 hours.[97] Furthermore, Liu et al. synthesized double-shelled hybrid carbon nanocages from epitaxially grown ZIF-67 crystals over ZIF-8 (ZIF-8@ZIF-67). These nanocages, carbonized at 700 °C in a nitrogen atmosphere and followed by acid washing, achieved a specific surface area of 467 $m^2 g^{-1}$.[93] The ZIF-67-derived materials exhibited high surface areas and excellent catalytic performance due to the controlled decomposition process that retained the hierarchical porosity and introduced nitrogen doping, crucial for ORR activity.

Our research team has made significant strides in developing several novel TAL MOFs, including Fe/Co/Ni/Mn-TAL, and bi- and trimetallic variants like FeNi, FeCo, MnCo, and FeNiCo. TAL-42—a mixed-metal manganese/cobalt variant—highlights the benefits of MOF-derived M-N-C catalysts.[77] These materials offer customizable functionalities, varied morphologies, and promising chemical and mechanical stabilities. Using MOFs as precursors allows for the tailoring of pore structure distribution, providing a high density of active sites and enhanced mass transfer.[77] Moreover, recent studies suggest that introducing secondary transition metals can significantly enhance bifunctional electrocatalytic performance by modifying the coordination environment of active centers.[77]

Bimetallic MOF materials leverage the synergistic effects of multiple metals to enhance catalytic performance. Bimetallic combinations like FeNi and MnCo have shown superior stability and activity, benefiting from the unique electronic and structural properties imparted by each metal.[77] Understanding the mechanistic aspects of these catalysts at the atomic level will help in designing even more efficient materials for various electrocatalytic applications.

In recent work, a series of transition-metal-doped ZIF-8 combined with carbon nanotube (CNT) composite catalysts (ZIF-8@CNT) were synthesized.[98] Obtained binary-metal-doped catalysts, demonstrated impressive half-wave potentials ($E_{1/2}$) of 0.846 and 0.847 V vs. RHE, respectively, surpassing the performance of commercial Pt/C catalysts ($E_{1/2}$ = 0.834 V). This approach highlights the potential of Zn-MOF-assisted synthesis in creating high-performance, cost-effective M-N-C materials for AEMFC applications.

In this work I explore using zinc-based metal-organic frameworks (Zn-MOFs), to assist in the synthesis of M-N-C materials. These Zn-MOFs are particularly effective because, upon pyrolysis, they produce high surface area carbon structures with well-dispersed nitrogen and

metal sites. The zinc component volatilizes during pyrolysis, leaving behind a porous carbon network doped with nitrogen, which enhances the catalytic activity and durability of the resulting materials.[98]

## 1.8 Cyclic Voltammetry and Rotating Disk Electrode Studies

Cyclic voltammetry (CV) is a fundamental electrochemical technique widely used to study the current response of an electrochemical cell when an applied voltage exceeds the value predicted by the Nernst equation. The essential components required for CV analysis include an electrolysis cell, a potentiostat, a current-to-voltage converter, and a data collection system. The electrolysis cell comprises four primary parts: the working electrode, counter electrode, reference electrode, and electrolyte solution.[99,100]

During a CV experiment, the voltage applied to the working electrode is varied cyclically, while the resultant current is recorded. The potential of the working electrode changes linearly, and the reference electrode maintains a constant potential. The resultant current-voltage plot, known as a cyclic voltammogram, provides valuable insights into the electrochemical processes occurring at the working electrode.[101,102]

The counter electrode facilitates the flow of current from the signal source to the working electrode, and the electrolytic solution supplies the necessary ions for oxidation and reduction reactions. The potentiostat, an electronic device, uses a direct current (DC) power supply to establish and control a specific potential, enabling the system to handle very small currents without altering the voltage. A current-to-voltage converter measures the resulting current, and a data-collecting system produces the voltammogram.[99,100]

CV is particularly useful for investigating qualitative aspects of electrochemical reactions under various conditions. It helps in identifying intermediates in redox reactions and assessing reaction reversibility. In a reversible Nernstian system, there is a direct correlation between concentration and current, allowing for the determination of unknown solute concentrations by constructing a calibration curve relating current to concentration. Additionally, CV can determine electron stoichiometry, diffusion coefficients of analytes, and formal redox potentials, making it an effective tool for both identification and analysis of electrochemical systems.[101,102]

The Rotating Disk Electrode (RDE) is an indispensable tool in the field of electrochemistry, particularly for studying the kinetics and mechanisms of electrocatalytic reactions such as the

ORR.[103] The RDE's capability to precisely measure reaction parameters and identify intermediate species is crucial in the development of electrocatalysts, aiding advancements in fuel cells and related technologies.[104] Understanding the kinetics and mechanisms of ORR, facilitated by various catalysts, is essential for the progression of these technologies, making RDE a cornerstone in electrocatalyst research.[105,106]

The principles of RDE operation are rooted in creating a well-defined hydrodynamic flow, achieved by rotating the disk-shaped electrode at controlled speeds within an electrolyte solution. This rotation helps eliminate natural convection, leading to steady-state conditions. Linear sweep voltammetry (LSV), commonly used with RDE, generates current-voltage curves that provide detailed information about the electrochemical reactions occurring at the electrode surface. The Levich equation quantitatively describes the relationship between the limiting current and the electrode rotation rate, which is fundamental in analyzing diffusion-controlled processes and determining kinetic parameters.[106,107]

The application of RDE extends beyond ORR to include the OER and the hydrogen evolution raction (HER). In OER studies, RDE helps measure overpotentials and assess catalyst performance under controlled hydrodynamic conditions, minimizing mass transport limitations.[107]

# 2 THE AIMS OF THE THESIS

Aim #1. To synthesize bifunctional oxygen electrocatalyst through carbonization of Fe/Co-Zn-coordinated TAL materials.

Aim #2. To physicochemically characterize prepared catalyst materials using XRD, $N_2$-physisorption, TEM, XPS, and MP-AES.

Aim #3. To study the electrochemical behaviour of prepared catalysts toward oxygen reduction and evolution reactions.

Aim #4. To relate the revealed structural characteristics and composition to the exhibited ORR, OER, and bifunctional performance values.

# 3 EXPERIMENTAL PART

## 3.1 MATERIALS AND METHODS

### 3.1.1 Chemicals and materials

Iron (III) chloride hexahydrate ($FeCl_3 \cdot 6H_2O$, ≥ 98%, Sigma-Aldrich), cobalt (II) chloride hexahydrate ($CoCl_2 \cdot 6H_2O$, ≥ 98%, Sigma-Aldrich), zinc chloride ($ZnCl_2$, ≥ 98%, Honeywell), ammonium hydroxide solution ($NH_3$ in $H_2O$, 25%, Lach-ner), N,N-Dimethylformamide (C3H7NO, ≥ 99,8%, Sigma-Aldrich) were used a received. All solutions were prepared using ultrapure water (18.2 MΩ cm) obtained from the Milli-Q purification system by Millipore. The post-synthetic carbonization of electrocatalysts was carried out using a tube furnace (Carbolite Gero EST 12/300B).

### 3.1.2 Synthesis

**1H-benzo[d]imidazole-5,6-diol** ligand was synthesized according to the previously published procedure.[108]

**Zn-TAL:** The preparation of Zn-TAL involved adding $ZnCl_2$ (1.38 g, 10.1 mmol, 0.5 equiv) dropwise into a mixture of 1H-benzo[d]imidazole-5,6-diol (3.0 g, 20.2 mmol, 2.0 equiv) in 25% aq.$NH_3$/DMF/EtOH/water (4:10:10:15; 50 mL). The resultant solution was stirred at room temperature (RT) for 24 hours, followed by filtration, EtOH washing, and overnight drying at 60 °C. Zn-TAL final mass = 0.83 g.

**FeZn-TAL:** A solution containing $FeCl_3 \cdot 6H_2O$ (0.45 g) and $ZnCl_2 \cdot 6H_2O$ (0.40 g) in water (5.8 mL) was gradually added dropwise to a mixture of 1H-benzo[d]imidazole-5,6-diol (1.00 g) in 25% aqueous $NH_3$/DMF/EtOH (1.5 mL, 3.8 mL, 3.8 mL). The resulting solution was stirred at RT for 24 hours, filtered, EtOH washed, and then dried overnight at 60 °C. Post-synthesis mass: 0.67 g (from 1 g of ligand).

**Fe-N-C:** The pyrolysis of FeZn-TAL (150 mg) was carried out under $N_2$ flow for 1 hour at 900 °C with a heating rate of 20 °C $min^{-1}$. The resulting product underwent acid etching with 3M HCl overnight at RT, followed by washing with deionized water until reaching neutral pH and drying at 60 °C for 24 hours. Subsequently, a second pyrolysis was conducted under the same conditions. Post-pyrolysis product mass: 30 mg.

**CoZn-TAL:** A solution comprising $CoCl_2 \times 6H_2O$ (0.40 g) and $ZnCl_2 \times 6H_2O$ (0.40 g) in water (5.8 mL) was added dropwise to a mixture of 1H-benzo[d]imidazole-5,6-diol (1.00 g) in 25% aqueous $NH_3$/DMF/EtOH (1.5 mL, 3.8 mL, 3.8 mL). After stirring at RT for 24 hours, the

resulting solution was filtered, washed with EtOH, and then dried overnight at 60 °C. Post-synthesis mass: 1.52 g (from 1 g of ligand).

**Co-N-C:** CoZn-TAL (334 mg) underwent pyrolysis under $N_2$ flow for 1 hour at 900 °C with a heating rate of 20 °C $min^{-1}$. Subsequently, the resulting product was acid etched with 3M HCl overnight at RT, washed with deionized water until neutral pH, and dried at 60 °C for 24 hours. Second pyrolysis was conducted under identical conditions. Post-pyrolysis product mass: 35 mg.

**FeCoZn-TAL:** A solution containing $CoCl_2$×6H2O (0.20 g), $FeCl_3$×$6H_2O$ (0.20 g), and $ZnCl_2$×$6H_2O$ (0.40 g) in water (5.8 mL) was gradually added dropwise to a mixture of 1H-benzo[d]imidazole-5,6-diol (1.00 g) in 25% aqueous $NH_3$/DMF/EtOH (1.5 mL, 3.8 mL, 3.8 mL). After stirring at RT for 24 hours, the resulting solution was filtered, washed with EtOH, and dried overnight at 60 °C. Post-synthesis mass: 1.43 g (from 1 g of ligand).

**FeCo-N-C:** CoFeZn-TAL (323 mg) was subjected to pyrolysis under $N_2$ flow for 1 hour at 900 °C with a heating rate of 20 °C $min^{-1}$. Product was acid etched with 3 M HCl overnight at RT, washed with deionized water until neutral pH, and dried at 60 °C for 24 hours. A second pyrolysis was performed under the same conditions. Post-pyrolysis product mass: 77 mg.

### 3.1.3 Physical characterization

PXRD analysis was conducted using a Bruker D8 Advance diffractometer equipped with a Ni-filtered Cu Kα as a radiation source and LynxEye line detector. Powder samples were scanned over a range of 3° to 93° 2θ with a scanning step of 0.013° 2θ and a counting time of 356 s per step.

XPS analysis was conducted under ultra-high vacuum conditions utilizing a non-monochromatic twin anode X-ray tube (Thermo XR3E2) with a characteristic energy of 1,253.6 eV (Mg Kα) and an electron energy analyzer SCIENTA SES 100. Samples were prepared by depositing a suspension of catalytic materials in isopropanol at a concentration of 4 mg $mL^{-1}$ onto GC plates measuring 1.1×1.1 cm. The survey scan covered an energy range from 900 to 0 eV, with a pass energy of 200 eV, step size of 0.5 eV, step duration of 0.2 s, and a scan number of 5. High-resolution XPS scans were performed using a pass energy of 200 eV and step size 0.1 eV. An Ag wire attached to the sample holders served as the energy reference (Ag 3d5/2 at 367.8 eV), and no charging effects were observed. Peak fitting was conducted using CasaXPS (version 2.3.16), employing the Gauss–Lorentz hybrid function

(GL 70, Gauss 30%, Lorentz 70%) and a blend of linear and Shirley-type backgrounds for peak fitting.

The concentration of metals in the bulk of the catalyst samples was analyzed using MP-AES with an Agilent 4210 instrument. Sample preparation involved microwave digestion conducted with an Anton Paar Multiwave PRO system to dissolve 10 mg of each catalyst material in a mixture of 2 mL of $H_2O_2$ and 4 mL of $HNO_3$ in NXF100 vessels with PTFE/TFM liner. The digestion parameters were as follows: temperature – 230 °C, pressures ranging from 45 to 50 bar. Subsequently, the digested samples were diluted to a metal concentration of 5 mg $L^{-1}$ of metal concentration was carried out with 2% $HNO_3$.

The porosity parameters of the prepared materials were assessed using low-temperature N2 adsorption with a NOVAtouch LX2 instrument from Quantachrome Instruments. Prior to measurement, each sample underwent degassing in a vacuum at 300 °C for 12 hours. The BET surface area ($S_{BET}$) of the materials was determined within a $P/P_0$ interval of 0.02 - 0.2, while the total pore volume ($V_{tot}$) was calculated with a value of $P/P_0$ of 0.97. Density functional theory (DFT) data, including specific surface area ($S_{dft}$), the volume of micropores (Vμ), and pore size distributions (PSD), were estimated from $N_2$ isotherms using a quenched solid density functional theory (QSDFT) equilibria model designed for slit-type pores.

The morphological structure of the synthesized materials was analyzed using scanning transmission electron microscopy (STEM), which provided high-angle annular dark field (HAADF) images along with energy dispersive X-ray spectroscopy (EDS) mapping.

### 3.1.4 Electrochemical characterization

**Ink preparation**

The catalyst ink for electrode modification was prepared by subjecting 5 mg of catalyst material, 5 μL of Nafion ionomer solution (5 wt%, Sigma-Aldrich), and 495 μL isopropyl alcohol to a 20-minute sonication process to ensure a uniform mixture.

**Electrode modification**

Before any modifications, the Teflon-embedded glassy carbon (GC) disk underwent polishing using 0.3 μm alumina slurry (Buehler). Subsequently, the electrode underwent a cleaning process by immersing it in an ultrasonic bath containing Milli-Q water and isopropyl alcohol

for 5 minutes to remove any residual alumina. Following this, the electrode was rinsed with water and then dried to eliminate any remaining moisture. A catalyst suspension was dispensed onto the GC area in five 2 μL increments, totaling 10 μL. The electrode was then dried in an oven set at 60 °C for 1-2 minutes, and then air-dried for at least 10 minutes.

**Electrochemical measurements**

The materials' electrochemical catalytic activity was evaluated using a standard three-electrode cell system connected to the Autolab PGSTAT128N potentiostat/galvanostat (Metrohm Autolab B.V., The Netherlands) and managed by Nova 2.1.4 software. For this investigation, the working electrode employed was a glassy carbon rotating disk electrode, specifically the OrigaTip model, with a diameter of 5 mm. A silver-silver chloride electrode served as the reference electrode, while a GC rod was utilized as the counter electrode. The alkaline electrolyte solution was prepared by dissolving 2.8 g of KOH (with a purity of at least 99.998%, sourced from Sigma-Aldrich) in 500 mL of Milli-Q water. The electrolyte was then saturated with either pure oxygen (99.999%, Linde Gas) or deaerated using argon gas (99.999%, Linde Gas).

ORR polarization curves obtained under $O_2$-saturated 0.1 M KOH electrolyte conditions, employing a scan rate of 10 mV $s^{-1}$ and varying rotation speeds (including 1600 rpm). Following this, an assessment of the OER activity was performed in an Ar-saturated electrolyte with 0.1 M KOH, utilizing a scan rate of 10 mV $s^{-1}$. Electrochemical data for OER underwent an 85% iR compensation. Conversion of potentials to RHE was conducted using the following formula:

$E_{Ag/AgCl} = E_{RHE} - 0.966$ ($E_{vs.RHE} = E_{vs.Ag/AgCl} + 0.0591*pH + E_{Ag/AgCl}^{\theta}$ (0.209))

The polarization curves were used to extract the key kinetic parameters of the ORR, specifically $E_{onset}$ and $E_{1/2}$, which denote the onset and half-wave potentials, respectively. The overall bifunctional activity of the oxygen electrode was measured as the potential difference ($\Delta E$) between the ORR half-wave potential and an OER current density of 10 mA $cm^{-2}$ ($E_{j=10}$), expressed as $\Delta E = E_{j=10} - E_{1/2}$.

## 3.2 RESULTS AND DISCUSSION

### 3.2.1 Synthesis and characterization

The choice of ligand is critical for the catalyst precursor, as it greatly affects the catalyst's activity, selectivity, and stability.[109] In this synthesis, the ligand 1H-benzo[d]imidazole-5,6-diol was selected for its rich carbon and nitrogen content and additional functional groups that enhance its ligating capabilities.[109] After dissolving the ligand, zinc chloride, iron(III) chloride, and cobalt(II) chloride were gradually added (Fig. 4), causing a color transition from colorless to orange-reddish, which signaled that the reaction inside the flask had occurred. Subsequently, the Fe/CoZn-TAL was pyrolyzed, resulting in the formation of M-N-C hollow spheres. After pyrolysis, the final product FeCo-N-C derived from Fe/CoZn-TAL exhibited excellent mesoporosity, high surface area, and electrochemical activity due to their unique asymmetric structures.[108]

The efficiency of the final product was a major consideration in selecting metals for the catalyst. Zn-derived M-N-C catalysts have shown good activity and stability.[110–112] However, the most remarkable property of Zn-based metal-organic precursors is zinc's ability to evaporate at 625 ℃.[113] During pyrolysis, non-coordinated zinc atoms tend to form agglomerates, which reduce surface area and promote catalytic graphitization.[113] In this study, zinc evaporation played a crucial role. Therefore, conducting pyrolysis at high temperatures allowed the evaporation of unstable zinc agglomerates, retaining $ZnN_x$ single-atom sites and preventing graphitization, thus maintaining the porous carbon hollow sphere framework.[113]

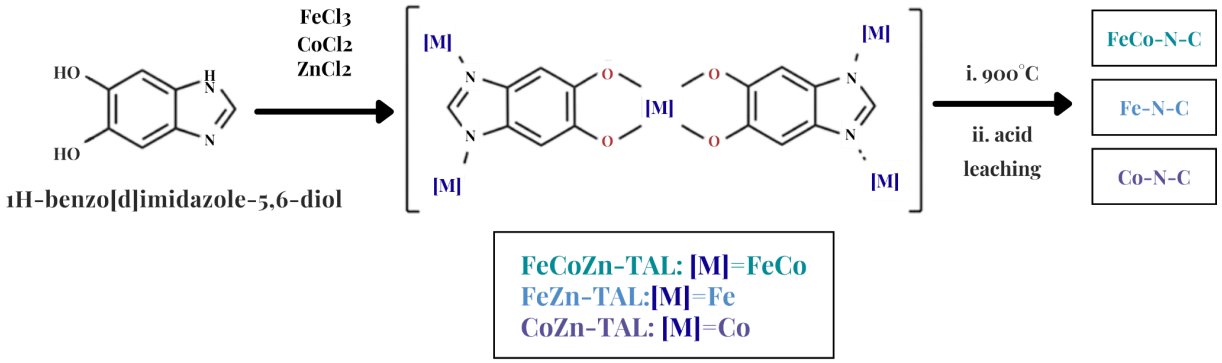


**Figure 4.** Synthesis of M–N–C catalyst materials.

### Physicochemical characterization

The morphological structure of synthesized materials was studied by scanning transmission electron microscopy (STEM) with high-angle annular dark field (HAADF) images together

with energy dispersive X-ray spectroscopy (EDS) mapping. STEM images in Fig. 5a show that materials are homogeneous and metal nanoparticles with an average diameter of 10 nm are well distributed with the M-N-C catalysts structure (Fig. 5b). The uniform distribution of nitrogen, oxygen, and corresponding metals in the selected regions was validated by (EDS) elemental mapping coupled with STEM (Fig. 6). EDS also showed that Zn residuals were present in all samples.

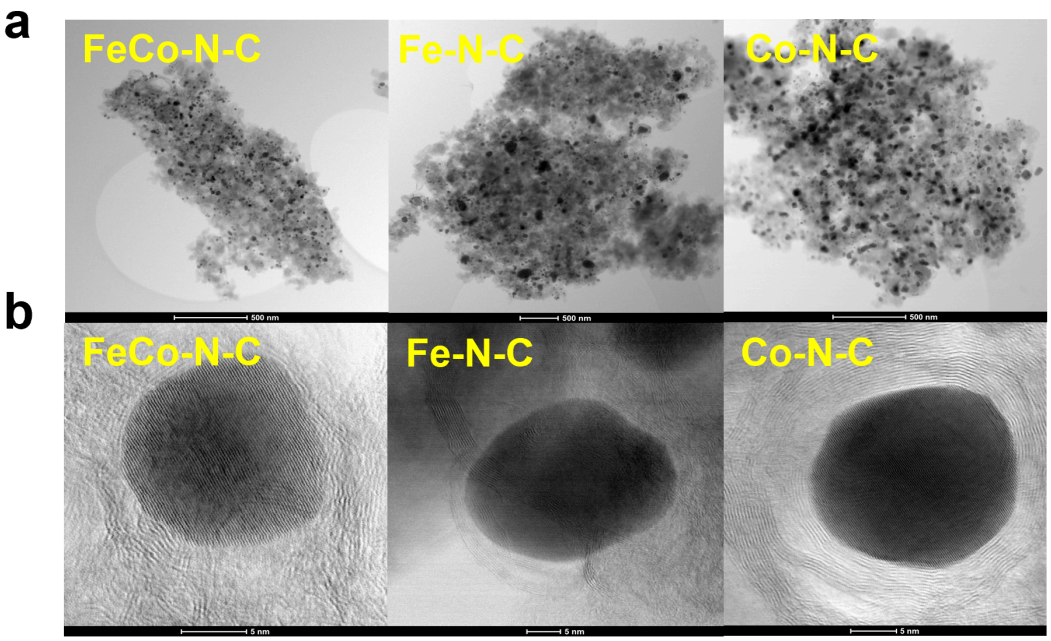


**Figure 5.** a) TEM and b) HR-TEM images of the FeCo–N–C, Co–N–C, and Fe–N–C samples

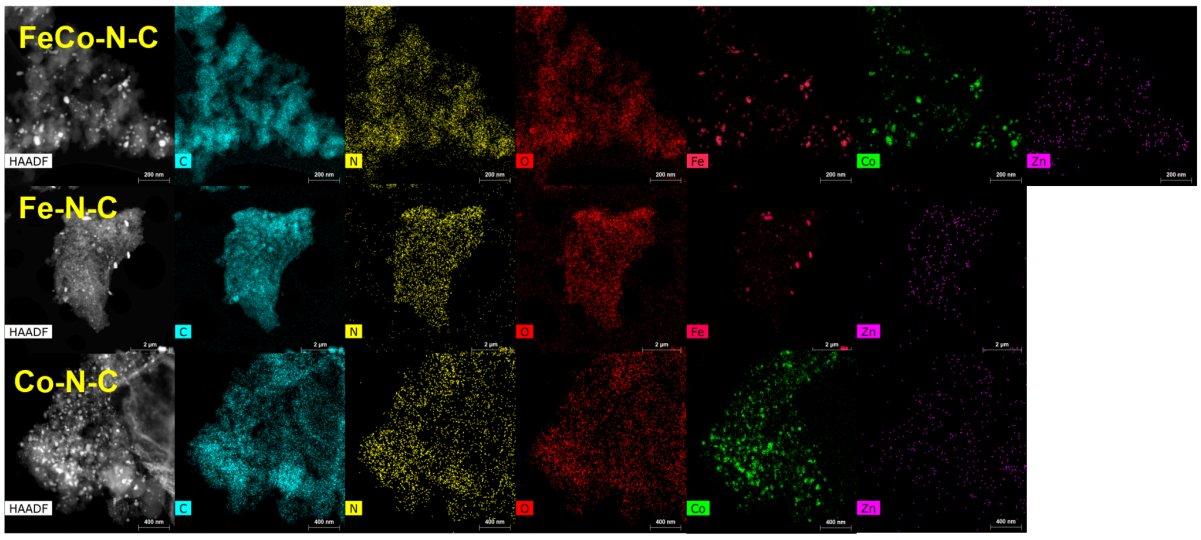


**Figure 6.** HAADF-STEM images, EDX mapping of FeCo–N–C, Co–N–C, and Fe–N–C materials.

According to X-ray diffraction (XRD) analysis (Fig. 7a), the characteristic peak of graphite-2H carbon (PDF 01-075-1621) can be seen from diffractograms of FeCo-N-C, Fe-N-C and Co-N-C at 26.4°, 44.5° and 54.06°. The primary crystalline phases of FeCo-N-C were syn-wairauite (PDF 00-044-1433) and iron oxide (PDF 01-090-3358), while α-Co (PDF 04-007-7986), CoO (PDF 04-006-1772) and $Co(N(CN)_2)_2$ (PDF 01-088-9565) are found in Co-N-C. The iron was present in the form of syn-cohenite (PDF 00-035-0772), Fe (PDF 04-013-9827), and $Fe_3O_4$ (PDF 04-015-8213) in Fe-N-C.

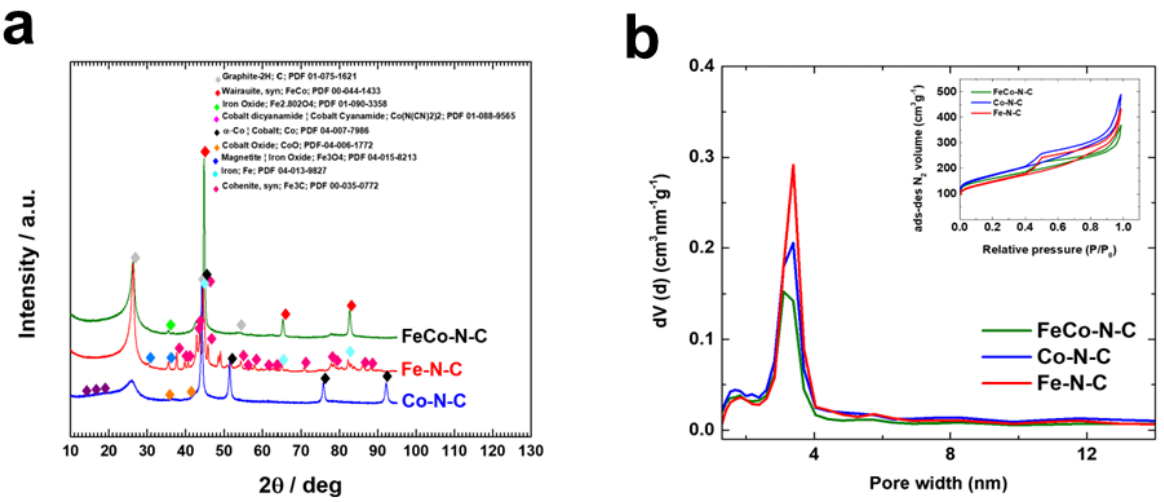


**Figure 7**. a) XRD diffractograms, b) gas adsorption isotherms and pore size distribution of FeCo-N-C, Co-N-C, and Fe-N-C samples.

$N_2$ physisorption analysis was applied to comprehend the textural properties of studied materials (Fig. 7b). Type-IV isotherms with H4 hysteresis loops were dominant in FeCo-N-C, Co-N-C, and Fe-N-C in the relative pressure range of 0.4 - 1.0. As seen from pore-size distribution curves, all samples possess micropores and mesopores which are favorable for enhancing the electrocatalytic performance by increasing the transport of reactants and reaction products. The highest surface area belonged to Co-N-C (603 $m^2 g^{-1}$) (Table 1).

**Table 1.** Textural properties of FeCo-N-C, Fe-N-C and Co-N-C.

| **Catalyst** | **$S_{BET}$ ($m^2 g^{-1}$)** | **$S_{DFT}$ ($m^2 g^{-1}$)** | **$V_{tot}$ ($cm^3 g^{-1}$)** | **$V_{\mu}$ ($cm^3 g^{-1}$)** |
|---|---|---|---|---|
| **FeCo-N-C** | 561 | 589 | 0.475 | 0.188 |
| **Fe-N-C** | 513 | 551 | 0.558 | 0.153 |
| **Co-N-C** | 603 | 640 | 0.611 | 0.192 |

X-ray photoelectron spectroscopy (XPS) was employed to investigate the surface elemental composition of the prepared samples. XPS survey spectra (figure not shown) indicated the presence of Fe and Co metals at the surface of catalysts which was validated with HAADF-STEM elemental mapping above. The atomic percentage of Fe was found to be 0.2% in both FeCo-N-C and Fe-N-C, while the amount of Co and N species was higher in Co-N-C (Co 1.2%; N 4.0 %) than in FeCo-N-C (Co 0.4%; N 3.0%) (Table 2).

Furthermore, microwave plasma-atomic emission spectroscopy (MP-AES) revealed that the bulk Co metal content was about four times higher in Co-N-C (17.64 wt%) material compared to FeCo-N-C (4.14 wt%), while bulk Fe content was two times higher in Fe-N-C (6.39 w%) than FeCo-N-C (3.29 w%) (Table 2).

High-resolution N 1s spectra showed the presence of pyrrolic, pyridinic, graphitic, and iminic groups and their distribution is shown in Figure 10. The metal-coordinated nitrogen species ($M{-}N_{x)}$ were found in all samples at 399.2 eV. The presence of various nitrogen functionalities in M-N-C-type materials is advantageous because each one contributes to distinct kinetic steps in the ORR.[114] The high-resolution Fe 2p spectra (Fig. 9b), revealed the presence of $FeO_x$, Fe met, and Fe 2p species in Fe-N-C and FeCo-N-C, while Co 2p photoelectron spectra showed $CoO_x$ and Co met species in Co-N-C and FeCo-N-C samples (Fig 9a). The presence of Fe and Co atoms catalyze the graphitization of the carbon skeleton and improve the electron conductivity of catalysts. Moreover, Fe and Co finely change the surface area and mesoporous structure to optimize exposed active sites and enhance the transfer of reactants.[115] Figure 8c displays various types of oxygen species in the O 1s region in all samples, likelylikely due to water and/or oxygen molecule adsorption onto the carbon surface.[115]

**Table 2.** The surface elemental composition (studied by XPS) and bulk metal composition (analyzed with MP-AES) of FeCo-N-C, Fe-N-C, and Co-N-C.

| **Sample** | **Surface elemental composition (at%)** | | | | | **Bulk metal composition (wt%)** | |
|---|---|---|---|---|---|---|---|
| | **C** | **N** | **O** | **Fe** | **Co** | **Fe** | **Co** |
| **FeCo-N-C** | 93.9 | 3.0 | 2.7 | 0.2 | 0.4 | 3.29 | 4.14 |
| **Fe-N-C** | 95.5 | 1.8 | 2.5 | 0.2 | N/A | 6.39 | N/A |
| **Co-N-C** | 92.3 | 4.0 | 2.5 | N/A | 1.2 | N/A | 17.64 |

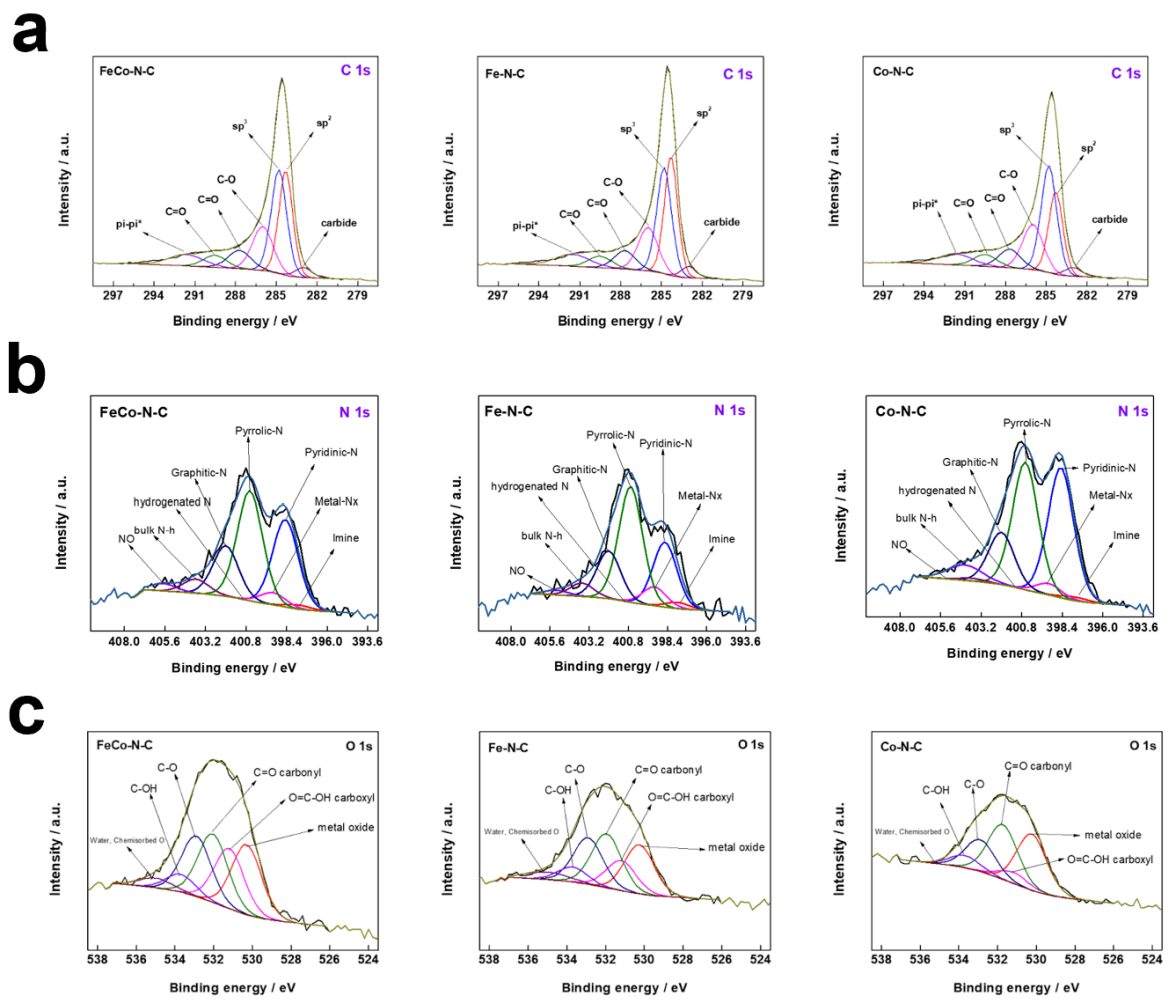


**Figure 8.** XPS high-resolution spectra in the C 1s, N 1s, and O 1s regions.

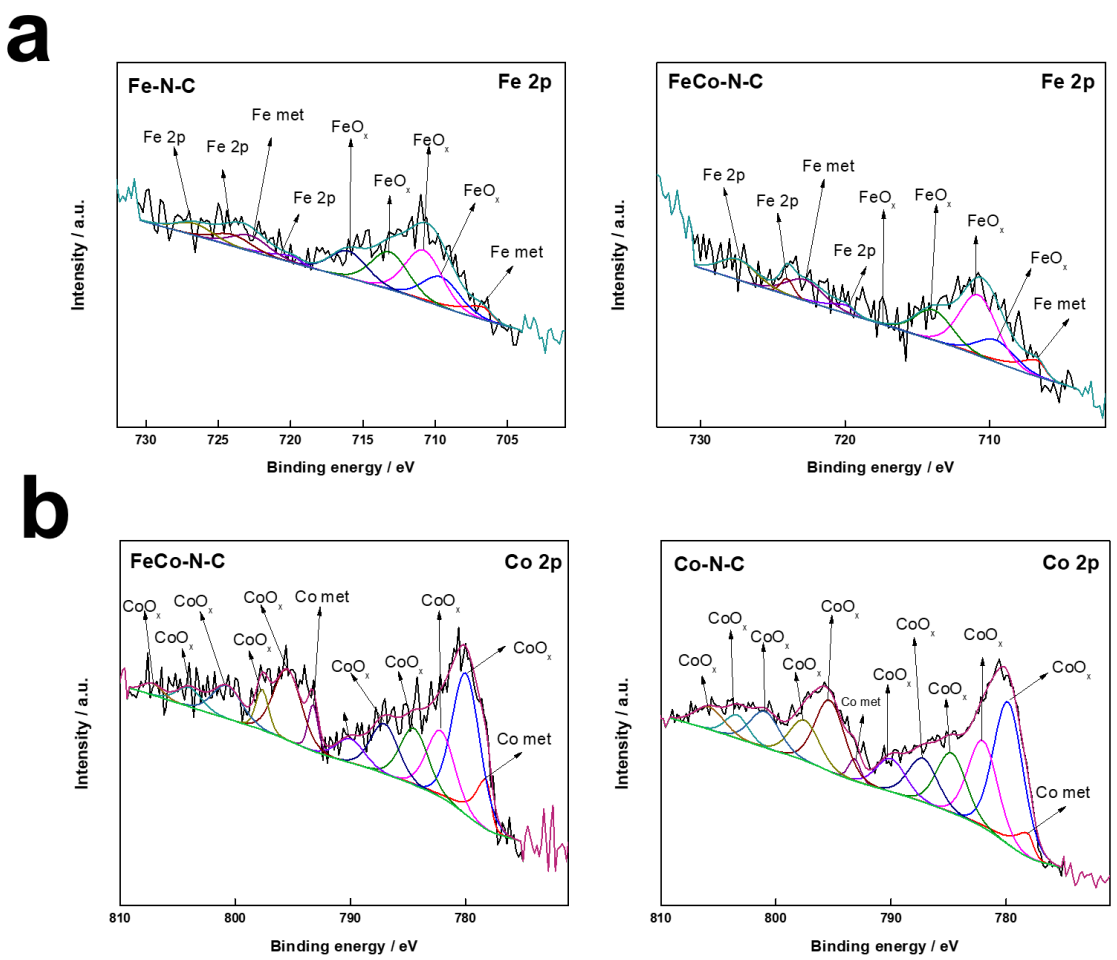


**Figure 9.** Deconvoluted high-resolution Fe 2p and Co 2p photoelectron spectra of Fe-N-C, Co-N-C, and FeCo-N-C catalysts.

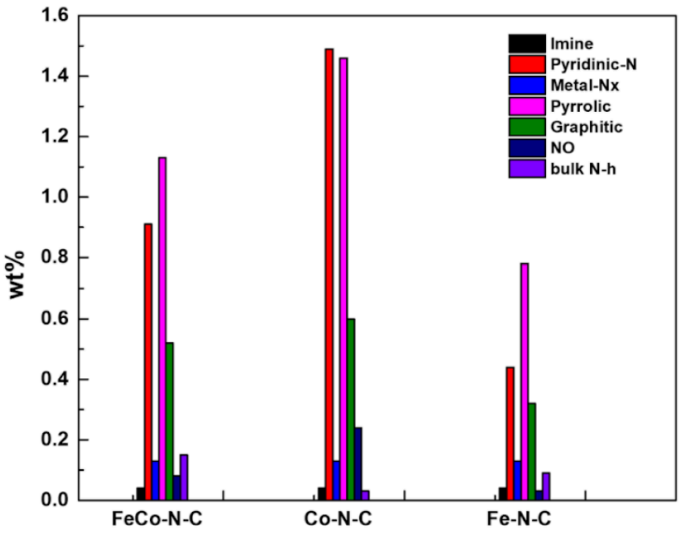


**Figure 10.** Distribution of nitrogen species in FeCo-N-C, Fe-N-C, and Co-N-C materials.

**Electrochemical characterization**

All three samples (FeCo-N-C, Fe-N-C, and Co-N-C) prepared in this work, together with commercial Pt/C and $RuO_2$ benchmarks, were studied as bifunctional ORR and OER. Figure 11 shows the CV scans recorded for all three catalysts in 0.1 M KOH solution, saturated with both Ar and $O_2$ gases, at a scan rate of 10 mV $s^{-1}$. The distinguishable reduction current peaks at ~ 0.80 V versus RHE were observed in an $O_2$-saturated electrolyte (Fig. 11).

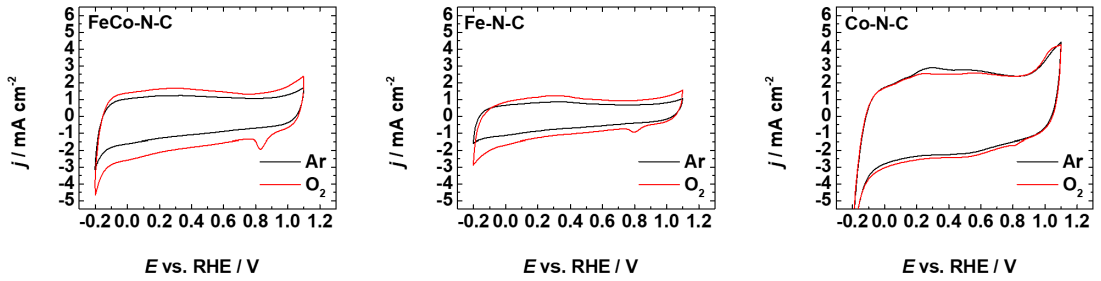


**Figure 11.** CV curves obtained for FeCo-N-C, Fe-N-C, and Co-N-C in $O_2$-saturated (red scan) or Ar-saturated (black scan) 0.1 M KOH solution.

To assess the ORR activity of prepared catalysts and the commercial Pt/C, the rotating disk electrode method was employed in the potential range of −0.2 to 1.1 V vs. RHE (Fig. 12a). The FeCo-N-C showed highest an onset potential of 0.99 V and a half-wave potential ($E_{1/2}$) of 0.85 V among all samples. This value was the same as that of the Pt/C ($E_{1/2}$=0.85 V vs. RHE). The Tafel slopes (Fig. 7b) derived from RDE data confirm an excellent ORR behavior. Co-N-C material has the lowest Tafel slope value (−38 mV $dec^{-1}$), indicating the faster ORR's kinetics on Co-N-C. Tafel slope values obtained for FeCo-N-C, Fe-N-C, and Co-N-C materials are comparable with previously reported iron, cobalt-doped carbon, and bimetallic FeCo N-C type catalysts.[74,88,115]

The electrochemical impedance spectroscopy technique was used to find charge-transfer kinetics and reached the value of 16 Ω for FeCo-N-C, Fe-N-C, and Co-N-C (Fig. 12e). To determine the number of electrocatalytically active sites, double-layer capacitance ($C_{dl}$) was constructed from electrochemical surface area (ECSA) scans at scan rates of 40 mV $s^{-1}$, 80 mV $s^{-1}$, 120 mV $s^{-1}$, 160 mV $s^{-1}$ and 200 mV $s^{-1}$. Surprisingly enough, Co-N-C reached the highest value of $C_{dl}$ (Fig. 12e) showing numerous active sites that enhance its ORR catalytic activity.

To evaluate the OER performance of the prepared catalysts alongside benchmark $RuO_2$, linear sweep voltammetry experiments were conducted in an argon-saturated 0.1 M KOH solution at

a rotation speed of 1600 rpm (Fig. 12c). In the case of Co-N-C modified GC electrode, the current density of 10 mA $cm^{-2}$ was reached at $E_{j=10}$ = 1.56 V vs. RHE. The corresponding overpotential value ($\eta$) was lower than that obtained for FeCo-N-C, Fe-N-C, and commercial $RuO_2$ (0.33 vs. 0.35, 0.39, and 0.46 V, accordingly) (Table 3). To investigate the OER mechanism on prepared catalysts, Tafel plots were calculated using the OER data. FeCo-N-C showed the lowest Tafel slope value (36 mV $dec^{-1}$), which indicated faster OER kinetics (Fig. 12d).

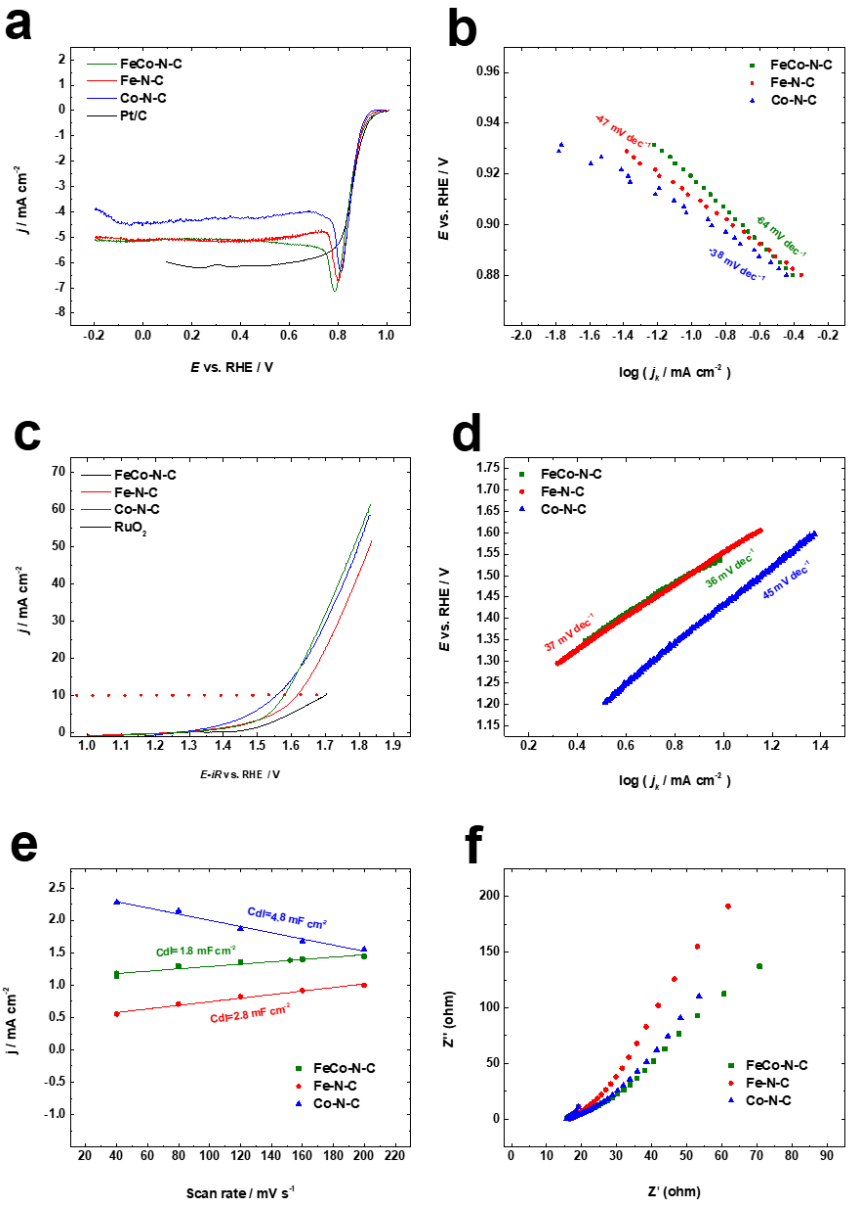


**Figure 12.** a) ORR scans obtained for FeCo-N-C, Fe-N-C, and Co-N-C in oxygen saturated 0.1 M KOH at 1600 rpm; (b) ORR Tafel plots; (c) LSV curves at 1600 rpm in Ar-saturated 0.1 M KOH; (d) OER Tafel plots; (e) The calculated capacitive currents as a function of scan rate; (f) EIS curves of all catalysts.

The overall oxygen bifunctional electroactivity of the prepared electrocatalysts was assessed by measuring the difference ($\Delta E$) between $E_{1/2}$ and $E_{j=10}$. Co-N-C exhibited the lowest $\Delta E$ value of 0.70 V among all the materials studied, including the commercial Pt/C + $RuO_2$ catalyst hybrid. The double-layer capacitance ($C_{dl}$) measurements (Fig. 12e) display $C_{dl}$ values of 1.8, 2.8, and 4.8 mF $cm^{-2}$ for FeCo-N-C, Fe-N-C, and Co-N-C, respectively. A higher $C_{dl}$ value of Co-N-C indicates better active site exposure to the electrolyte.

**Table 3.** The ORR and OER kinetic parameters were obtained for all electrocatalyst materials in 0.1 M KOH solution.

| **Catalyst** | $E_{1/2}$ **(V vs. RHE)** | $E_{on}$ **(V vs. RHE)** | $E_{j=10}$ **(V vs. RHE)** | $\Delta E$ **(V)** | **Tafel slope ORR (mV dec$^{-1}$)** | **Tafel slope OER (mV dec$^{-1}$)** | $\eta$**OER (V)** |
|---|---|---|---|---|---|---|---|
| **FeCo-N-C** | 0.85 | 0.99 | 1.58 | 0.73 | -64 | 36 | 0.35 |
| **Fe-N-C** | 0.86 | 0.97 | 1.62 | 0.76 | -47 | 37 | 0.39 |
| **Co-N-C** | 0.86 | 0.95 | 1.56 | 0.70 | -38 | 45 | 0.33 |
| **Pt/C+$RuO_2$** | 0.85 | 0.98 | 1.69 | 0.84 | -60 | 166 | 0.46 |

In a recent study, Wu et al. explored the coordination geometry of Fe-$N_4$ sites, demonstrating that pyrrolic-N coordination results in higher ORR activity than pyridinic-N coordination.[38] Their study used DFT calculations to show that the pyrrolic-N environment around Fe enhances electron depletion, leading to better $O_2$ and ORR intermediates' adsorption, promoting a complete four-electron reduction reaction. Jaouen et al. identified two types of Fe-$N_4$ sites in Fe-N-C electrocatalysts, emphasizing the importance of the local electronic structure.[116] Their *operando* 57Fe Mössbauer spectroscopy analysis showed that Fe-N-C contain two types of Fe-$N_x$ sites, which have similar isomer shifts. These studies revealed that a high-spin $FeN_4C_{12}$ moiety (pyrrole-type Fe-$N_4$) exhibits higher durability and ORR activity compared to pyridinic-type Fe-$N_4$. Research by Xie et al. focused on Co-$N_4$ sites and demonstrated that although these sites show promising activity, their adsorption energy for ORR intermediates is often too weak.[117] This limits the formation of intermediates, thus affecting the overall ORR kinetics. Their findings suggest that engineering the local geometry and incorporating heteroatoms can enhance the activity of Co-N-C catalysts.[117]

All three bifunctional catalysts underwent long-term ORR stability tests in an oxygen-saturated electrolyte in the range of 0.6 – 1.0 V vs. RHE at 100 mV $s^{-1}$ (Fig. 13). All

catalysts demonstrated exceptional ORR stability as indicated by the overlapping polarization curves before and after 5000 CV cycles (Fig. 13).

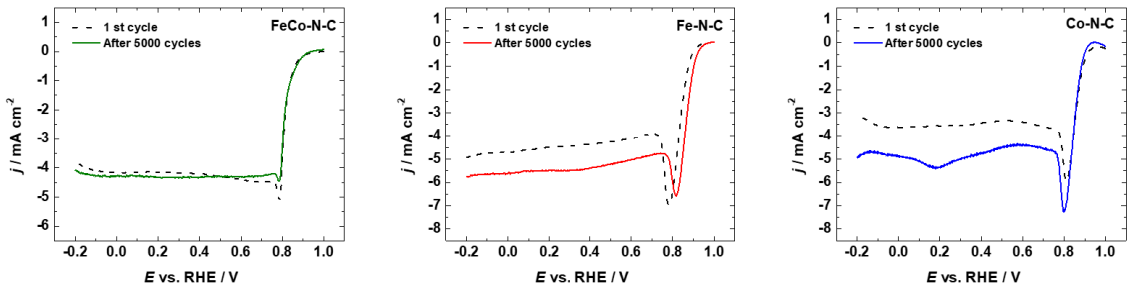


**Figure 13.** ORR polarization curves obtained before and after long-term potential cycling for FeCo-N-C, Fe-N-C, and Co-N-C.

### Zinc-air battery test

A rechargeable Zn-Air battery (ZAB) was assembled to assess the practical application where the air cathode is carbon paper-supported FeCo–N–C material. The charge-discharge polarisation curves in Fig. 14a exhibit that FeCo-N-C has a higher power density compared to the state-of-the-art Pt-Ru/C benchmark (159 mW $cm^{-2}$ vs. 79 mW $cm^{-2}$). The galvanostatic charge-discharge cycling performance of FeCo–N–C was contrasted with that of Pt-Ru/C in Figure 9b. The charge-discharge polarization curve showed that the initial discharging and charging potentials were 1.21 V, and 2.07 V. FeCo-N-C showed excellent stability for 14 h, with a potential window escalating due to the formation of ZnO. The performance of FeCo-N-C in ZAB assembly was compared with commercial Pt–$RuO_2$/C material, which showed lower peak power density (79 mW $cm^{-2}$) and a higher gap between the charging and discharging voltage (Fig 14b).

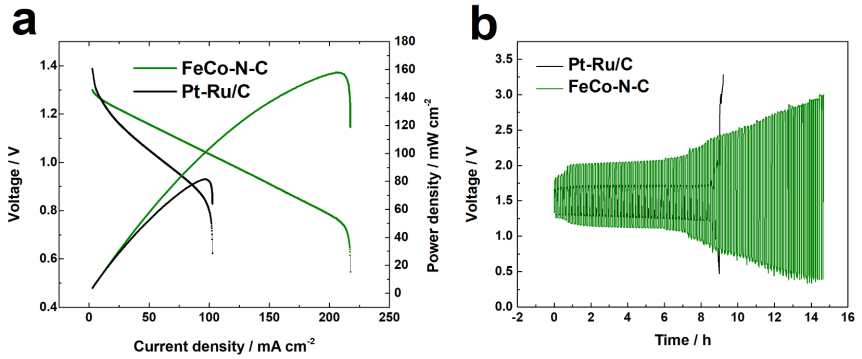


**Figure 14.** a) Polarisation and power density curves of FeCo-N-C and Pt-Ru/C catalysts. b) charge and discharge cycling results for the rechargeable ZABs.

## SUMMARY

This master thesis presents the development and characterization of a novel mixed-metal iron/cobalt/zinc-TAL metal-organic framework (MOF) as a versatile precursor for the fabrication of highly efficient bifunctional oxygen electrocatalysts. The synthesized TAL MOF, utilizing a benzimidazole ligand, undergoes pyrolysis at 900 °C to form porous M-N-C materials with intrinsic morphologies and high active site concentrations suitable for oxygen evolution reaction and oxygen reduction reaction. Detailed morphological and structural analyses were performed using advanced techniques, including scanning transmission electron microscopy, high-angle annular dark field imaging, and energy-dispersive X-ray spectroscopy mapping. The results confirmed the homogeneity and uniform distribution of metal nanoparticles within the M-N-C catalysts. X-ray diffraction further identified the crystalline phases, indicating the presence of metallic iron and cobalt and corresponding oxides in various samples. According to $N_2$ physisorption analysis, the highest surface area corresponded to the Co-N-C catalyst (603 $m^2\ g^{-1}$). X-ray photoelectron spectroscopy (XPS) and microwave plasma-atomic emission spectroscopy (MP-AES) were used to study surface and bulk compositions, highlighting the advantageous distribution of nitrogen functionalities and the catalytic roles of Fe and Co in enhancing graphitization and electron conductivity. Electrochemical characterization showed that FeCo-N-C, Fe-N-C, and Co-N-C catalysts exhibited excellent bifunctional activity for ORR and OER, outperforming commercial Pt/C and $RuO_2$ benchmarks in several metrics. Co-N-C demonstrated the fastest ORR kinetics and the highest double-layer capacitance, indicative of numerous active sites. FeCo-N-C showed the highest onset potential and comparable half-wave potential to Pt/C, as well as the lowest Tafel slope for OER, suggesting superior catalytic efficiency. The practical application of the FeCo-N-C catalyst was demonstrated in a rechargeable zinc-air battery, where it exhibited a higher power density and better stability than a commercial Pt-Ru/C catalyst.

This master thesis contributes to a significant advancement in the rational design and synthesis of multimetallic MOF-derived catalysts, highlighting their potential in renewable energy technologies.

## REFERENCES


1 T.-Z. Ang, M. Salem, M. Kamarol, H. S. Das, M. A. Nazari and N. Prabaharan, A comprehensive study of renewable energy sources: Classifications, challenges and suggestions, *Energy Strategy Rev.*, 2022, **43**, 100939.

2 A. Fauzi, X. Chen, H. Zhao, S. Cao, L. Kong, S. Huang, S. Zhang and X. Ma, Recent progress of M-N-C single atom electrocatalysts for carbon dioxide reduction reaction, *Energy*, 2023, **1**, 100045.

3 V. Cigolotti, M. Genovese and P. Fragiacomo, Comprehensive Review on Fuel Cell Technology for Stationary Applications as Sustainable and Efficient Poly-Generation Energy Systems, *Energies*, 2021, **14**, 4963.

4 J. Milikić, A. Nastasić, M. Martins, C. A. C. Sequeira and B. Šljukić, Air Cathodes and Bifunctional Oxygen Electrocatalysts for Aqueous Metal–Air Batteries, *Batteries*, 2023, **9**, 394.

5 G. A. K. M. R. Bari and J.-H. Jeong, Comprehensive Insights and Advancements in Gel Catalysts for Electrochemical Energy Conversion, *Gels*, 2024, **10**, 63.

6 D. Chen, J. Zhu, X. Mu, R. Cheng, W. Li, S. Liu, Z. Pu, C. Lin and S. Mu, Nitrogen-Doped carbon coupled FeNi3 intermetallic compound as advanced bifunctional electrocatalyst for OER, ORR and zn-air batteries, *Appl. Catal. B Environ.*, 2020, **268**, 118729.

7 X. Xu, S. Wang, S. Guo, K. San Hui, J. Ma, D. A. Dinh, K. N. Hui, H. Wang, L. Zhang and G. Zhou, Cobalt phosphosulfide nanoparticles encapsulated into heteroatom-doped carbon as bifunctional electrocatalyst for Zn−air battery, *Adv. Powder Mater.*, 2022, **1**, 100027.

8 H. Wang, C. Sun, E. Zhu, C. Shi, J. Yu and M. Xu, Core-shell MOF-derived Fe3C-Co-NC as high-performance ORR/OER bifunctional catalyst, *J. Alloys Compd.*, 2023, **948**, 169728.

9 C. Sealy, The problem with platinum, *Mater. Today*, 2008, **11**, 65–68.

10 J. Cui, Q. Chen, X. Li and S. Zhang, Recent advances in non-precious metal electrocatalysts for oxygen reduction in acidic media and PEMFCs: an activity, stability and mechanism study, *Green Chem.*, 2021, **23**, 6898–6925.

11 X. Liu, J. Huang, Q. Zhang and L. Mai, Nanostructured Metal Oxides and Sulfides for Lithium–Sulfur Batteries, *Adv. Mater.*, 2017, **29**, 1601759.

12 F. Dong, M. Wu, Z. Chen, X. Liu, G. Zhang, J. Qiao and S. Sun, Atomically Dispersed Transition Metal-Nitrogen-Carbon Bifunctional Oxygen Electrocatalysts for Zinc-Air Batteries: Recent Advances and Future Perspectives, *Nano-Micro Lett.*, 2022, **14**, 36.

13 C. Li, H. Zhang, M. Liu, F.-F. Lang, J. Pang and X.-H. Bu, Recent progress in metal–organic frameworks (MOFs) for electrocatalysis, *Ind. Chem. Mater.*, 2023, **1**, 9–38.

14 X. Chen, Z. Zhang, Y. Chen, R. Xu, C. Song, T. Yuan, W. Tang, X. Gao, N. Wang and L. Cui, Research advances in earth-abundant-element-based electrocatalysts for oxygen evolution reaction and oxygen reduction reaction, *Energy Mater.*, , DOI:10.20517/energymater.2023.12.

15 L. Fan, Z. Tu and S. H. Chan, Recent development of hydrogen and fuel cell technologies: A review, *Energy Rep.*, 2021, **7**, 8421–8446.

16 X. Cheng, Z. Shi, N. Glass, L. Zhang, J. Zhang, D. Song, Z.-S. Liu, H. Wang and J. Shen, A review of PEM hydrogen fuel cell contamination: Impacts, mechanisms, and mitigation, *J. Power Sources*, 2007, **165**, 739–756.

17 J. R. Varcoe, P. Atanassov, D. R. Dekel, A. M. Herring, M. A. Hickner, Paul. A. Kohl, A. R. Kucernak, W. E. Mustain, K. Nijmeijer, K. Scott, T. Xu and L. Zhuang, Anion-exchange membranes in electrochemical energy systems, *Energy Env. Sci*, 2014, **7**, 3135–3191.

18 S. Gottesfeld, D. R. Dekel, M. Page, C. Bae, Y. Yan, P. Zelenay and Y. S. Kim, Anion exchange membrane fuel cells: Current status and remaining challenges, *J. Power Sources*, 2018, **375**, 170–184.

19 B. P. Tripathi and V. K. Shahi, Organic–inorganic nanocomposite polymer electrolyte membranes for fuel cell applications, *Prog. Polym. Sci.*, 2011, **36**, 945–979.
20 V. Vijayakumar and S. Y. Nam, Recent advancements in applications of alkaline anion exchange membranes for polymer electrolyte fuel cells, *J. Ind. Eng. Chem.*, 2019, **70**, 70–86.
21 D. Li, E. J. Park, W. Zhu, Q. Shi, Y. Zhou, H. Tian, Y. Lin, A. Serov, B. Zulevi, E. D. Baca, C. Fujimoto, H. T. Chung and Y. S. Kim, Highly quaternized polystyrene ionomers for high performance anion exchange membrane water electrolysers, *Nat. Energy*, 2020, **5**, 378–385.
22 A. Holewinski, J.-C. Idrobo and S. Linic, High-performance Ag–Co alloy catalysts for electrochemical oxygen reduction, *Nat. Chem.*, 2014, **6**, 828–834.
23 T. Mo, Y. Li and Y. Luo, Advantages and Technological Progress of Hydrogen Fuel Cell Vehicles, *World Electr. Veh. J.*, 2023, **14**, 162.
24 A. Iqbal, O. M. El-Kadri and N. M. Hamdan, Insights into rechargeable Zn-air batteries for future advancements in energy storing technology, *J. Energy Storage*, 2023, **62**, 106926.
25 S. Hosseini, S. Masoudi Soltani and Y.-Y. Li, Current status and technical challenges of electrolytes in zinc–air batteries: An in-depth review, *Chem. Eng. J.*, 2021, **408**, 127241.
26 D. P. Trudgeon, K. Qiu, X. Li, T. Mallick, O. O. Taiwo, B. Chakrabarti, V. Yufit, N. P. Brandon, D. Crevillen-Garcia and A. Shah, Screening of effective electrolyte additives for zinc-based redox flow battery systems, *J. Power Sources*, 2019, **412**, 44–54.
27 T. Li, M. Huang, X. Bai and Y.-X. Wang, Metal–air batteries: A review on current status and future applications, *Prog. Nat. Sci. Mater. Int.*, 2023, **33**, 151–171.
28 N. Nitta, F. Wu, J. T. Lee and G. Yushin, Li-ion battery materials: present and future, *Mater. Today*, 2015, **18**, 252–264.
29 P. G. Bruce, S. A. Freunberger, L. J. Hardwick and J.-M. Tarascon, Li–O2 and Li–S batteries with high energy storage, *Nat. Mater.*, 2012, **11**, 19–29.
30 T. Liu, J. P. Vivek, E. W. Zhao, J. Lei, N. Garcia-Araez and C. P. Grey, Current Challenges and Routes Forward for Nonaqueous Lithium–Air Batteries, *Chem. Rev.*, 2020, **120**, 6558–6625.
31 S. Hosseini, H.-C. Fang, H. Pourzolfaghar, F. Mazari and Y.-Y. Li, The influence of S O anion groups of organic/inorganic additives in rechargeability of zinc-air batteries, *J. Energy Storage*, 2023, **67**, 107319.
32 C. W. Lee, K. Sathiyanarayanan, S. W. Eom, H. S. Kim and M. S. Yun, Novel electrochemical behavior of zinc anodes in zinc/air batteries in the presence of additives, *J. Power Sources*, 2006, **159**, 1474–1477.
33 J.-M. Assafrei, G. Yusibova, K. Ping, H.-M. Piirsoo, A. Tamm, M. Käärik, J. Leis, J. Aruväli, V. Grozovski, E. Lust and N. Kongi, Maximizing the performance of aqueous zinc-air/iodide hybrid batteries through electrolyte composition optimization, *J. Energy Storage*, 2023, **74**, 109528.
34 C. Wang, T. Wang, Q. Liu, W. Jia, X. Han and D. Wu, Starch-based porous carbon microsphere composited NiCo2O4 nanoflower as bifunctional electrocatalyst for zinc-air battery, *Int. J. Biol. Macromol.*, 2023, **241**, 124604.
35 J. Lilloja, M. Mooste, E. Kibena-Põldsepp, A. Sarapuu, A. Kikas, V. Kisand, M. Käärik, J. Kozlova, A. Treshchalov, P. Paiste, J. Aruväli, J. Leis, A. Tamm, S. Holdcroft and K. Tammeveski, Cobalt-, iron- and nitrogen-containing ordered mesoporous carbon-based catalysts for anion-exchange membrane fuel cell cathode, *Electrochimica Acta*, 2023, **439**, 141676.
36 J. Zhang, Y. Zhang, C. Xu, Y. Li, G. Ni, P. Huo, V. Balasubramani, Z. Li and B. Liu, Metal-organic-framework-derived bimetallic carbon-based catalysts as efficient oxygen reduction reaction electrocatalysts, *J. Alloys Compd.*, 2023, **948**, 169721.
37 X. Wu, H. Miao, R. Hu, B. Chen, M. Yin, H. Zhang, L. Xia, C. Zhang and J. Yuan, A-site

deficient perovskite nanofibers boost oxygen evolution reaction for zinc-air batteries, *Appl. Surf. Sci.*, 2021, **536**, 147806.
38 Y. Wu, X. Wu, T. Tu, P. Zhang, J. Li, Y. Zhou, L. Huang and S. Sun, Controlled synthesis of FeNx-CoNx dual active sites interfaced with metallic Co nanoparticles as bifunctional oxygen electrocatalysts for rechargeable Zn-air batteries, *Appl. Catal. B Environ.*, 2020, **278**, 119259.
39 Y. Li and H. Dai, Recent advances in zinc–air batteries, *Chem Soc Rev*, 2014, **43**, 5257–5275.
40 Z. Wu, M. Song, J. Wang and X. Liu, Recent Progress in Nitrogen-Doped Metal-Free Electrocatalysts for Oxygen Reduction Reaction, *Catalysts*, 2018, **8**, 196.
41 H. Liu, J. Guan, S. Yang, Y. Yu, R. Shao, Z. Zhang, M. Dou, F. Wang and Q. Xu, Metal–Organic‐Framework‐Derived $Co_2P$ Nanoparticle/Multi‐Doped Porous Carbon as a Trifunctional Electrocatalyst, *Adv. Mater.*, 2020, **32**, 2003649.
42 Z.-F. Huang, J. Song, S. Dou, X. Li, J. Wang and X. Wang, Strategies to Break the Scaling Relation toward Enhanced Oxygen Electrocatalysis, *Matter*, 2019, **1**, 1494–1518.
43 H. Li, S. Kelly, D. Guevarra, Z. Wang, Y. Wang, J. A. Haber, M. Anand, G. T. K. K. Gunasooriya, C. S. Abraham, S. Vijay, J. M. Gregoire and J. K. Nørskov, Analysis of the limitations in the oxygen reduction activity of transition metal oxide surfaces, *Nat. Catal.*, 2021, **4**, 463–468.
44 H.-Q. Chen, L. Zou, D.-Y. Wei, L.-L. Zheng, Y.-F. Wu, H. Zhang and J.-F. Li, In situ studies of energy-related electrochemical reactions using Raman and X-ray absorption spectroscopy, *Chin. J. Catal.*, 2022, **43**, 33–46.
45 S. C. Perry, D. Pangotra, L. Vieira, L.-I. Csepei, V. Sieber, L. Wang, C. Ponce De León and F. C. Walsh, Electrochemical synthesis of hydrogen peroxide from water and oxygen, *Nat. Rev. Chem.*, 2019, **3**, 442–458.
46 X. Ge, A. Sumboja, D. Wuu, T. An, B. Li, F. W. T. Goh, T. S. A. Hor, Y. Zong and Z. Liu, Oxygen Reduction in Alkaline Media: From Mechanisms to Recent Advances of Catalysts, *ACS Catal.*, 2015, **5**, 4643–4667.
47 R. Cepitis, V. Ivaništšev, J. Rossmeisl and N. Kongi, Bypassing the scaling relations in oxygen electrocatalysis with geometry-adaptive catalysts, *Catal. Sci. Technol.*, 2024, **14**, 2105–2113.
48 R. Cepitis, N. Kongi, J. Rossmeisl and V. Ivaništšev, Surface Curvature Effect on Dual-Atom Site Oxygen Electrocatalysis, *ACS Energy Lett.*, 2023, **8**, 1330–1335.
49 Z. Huang, J. Wang, Y. Peng, C. Jung, A. Fisher and X. Wang, Design of Efficient Bifunctional Oxygen Reduction/Evolution Electrocatalyst: Recent Advances and Perspectives, *Adv. Energy Mater.*, 2017, **7**, 1700544.
50 A. Kulkarni, S. Siahrostami, A. Patel and J. K. Nørskov, Understanding Catalytic Activity Trends in the Oxygen Reduction Reaction, *Chem. Rev.*, 2018, **118**, 2302–2312.
51 Z. W. Seh, J. Kibsgaard, C. F. Dickens, I. Chorkendorff, J. K. Nørskov and T. F. Jaramillo, Combining theory and experiment in electrocatalysis: Insights into materials design, *Science*, 2017, **355**, eaad4998.
52 J. Song, C. Wei, Z.-F. Huang, C. Liu, L. Zeng, X. Wang and Z. J. Xu, A review on fundamentals for designing oxygen evolution electrocatalysts, *Chem. Soc. Rev.*, 2020, **49**, 2196–2214.
53 L. Gao, X. Cui, C. D. Sewell, J. Li and Z. Lin, Recent advances in activating surface reconstruction for the high-efficiency oxygen evolution reaction, *Chem. Soc. Rev.*, 2021, **50**, 8428–8469.
54 D. W. Shaffer, Y. Xie and J. J. Concepcion, O–O bond formation in ruthenium-catalyzed water oxidation: single-site nucleophilic attack vs. O–O radical coupling, *Chem. Soc. Rev.*, 2017, **46**, 6170–6193.
55 M. J. Craig, G. Coulter, E. Dolan, J. Soriano-López, E. Mates-Torres, W. Schmitt and M.

García-Melchor, Universal scaling relations for the rational design of molecular water oxidation catalysts with near-zero overpotential, *Nat. Commun.*, 2019, **10**, 4993.
56 Y. Zhao, D. P. Adiyeri Saseendran, C. Huang, C. A. Triana, W. R. Marks, H. Chen, H. Zhao and G. R. Patzke, Oxygen Evolution/Reduction Reaction Catalysts: From *In Situ* Monitoring and Reaction Mechanisms to Rational Design, *Chem. Rev.*, 2023, **123**, 6257–6358.
57 A. J. Medford, A. Vojvodic, J. S. Hummelshøj, J. Voss, F. Abild-Pedersen, F. Studt, T. Bligaard, A. Nilsson and J. K. Nørskov, From the Sabatier principle to a predictive theory of transition-metal heterogeneous catalysis, *J. Catal.*, 2015, **328**, 36–42.
58 R. Christensen, H. A. Hansen, C. F. Dickens, J. K. Nørskov and T. Vegge, Functional Independent Scaling Relation for ORR/OER Catalysts, *J. Phys. Chem. C*, 2016, **120**, 24910–24916.
59 A. Vojvodic and J. K. Nørskov, New design paradigm for heterogeneous catalysts, *Natl. Sci. Rev.*, 2015, **2**, 140–143.
60 J. Wang, Y. Gao, H. Kong, J. Kim, S. Choi, F. Ciucci, Y. Hao, S. Yang, Z. Shao and J. Lim, Non-precious-metal catalysts for alkaline water electrolysis: *operando* characterizations, theoretical calculations, and recent advances, *Chem. Soc. Rev.*, 2020, **49**, 9154–9196.
61 H. Ding, H. Liu, W. Chu, C. Wu and Y. Xie, Structural Transformation of Heterogeneous Materials for Electrocatalytic Oxygen Evolution Reaction, *Chem. Rev.*, 2021, **121**, 13174–13212.
62 C. Walter, P. W. Menezes and M. Driess, Perspective on intermetallics towards efficient electrocatalytic water-splitting, *Chem. Sci.*, 2021, **12**, 8603–8631.
63 C. Baeumer, J. Li, Q. Lu, A. Y.-L. Liang, L. Jin, H. P. Martins, T. Duchoň, M. Glöß, S. M. Gericke, M. A. Wohlgemuth, M. Giesen, E. E. Penn, R. Dittmann, F. Gunkel, R. Waser, M. Bajdich, S. Nemšák, J. T. Mefford and W. C. Chueh, Tuning electrochemically driven surface transformation in atomically flat LaNiO3 thin films for enhanced water electrolysis, *Nat. Mater.*, 2021, **20**, 674–682.
64 J. Huang, L. Sementa, Z. Liu, G. Barcaro, M. Feng, E. Liu, L. Jiao, M. Xu, D. Leshchev, S.-J. Lee, M. Li, C. Wan, E. Zhu, Y. Liu, B. Peng, X. Duan, W. A. Goddard, A. Fortunelli, Q. Jia and Y. Huang, Experimental Sabatier plot for predictive design of active and stable Pt-alloy oxygen reduction reaction catalysts, *Nat. Catal.*, 2022, **5**, 513–523.
65 K. Wieszczycka, K. Staszak, M. J. Woźniak-Budych, J. Litowczenko, B. M. Maciejewska and S. Jurga, Surface functionalization – The way for advanced applications of smart materials, *Coord. Chem. Rev.*, 2021, **436**, 213846.
66 H. Li, H. Zhao, B. Tao, G. Xu, S. Gu, G. Wang and H. Chang, Pt-Based Oxygen Reduction Reaction Catalysts in Proton Exchange Membrane Fuel Cells: Controllable Preparation and Structural Design of Catalytic Layer, *Nanomaterials*, 2022, **12**, 4173.
67 Y. Nie, S. Chen, W. Ding, X. Xie, Y. Zhang and Z. Wei, Pt/C trapped in activated graphitic carbon layers as a highly durable electrocatalyst for the oxygen reduction reaction, *Chem Commun*, 2014, **50**, 15431–15434.
68 F. Xiao, Y. Wang, G.-L. Xu, F. Yang, S. Zhu, C.-J. Sun, Y. Cui, Z. Xu, Q. Zhao, J. Jang, X. Qiu, E. Liu, W. S. Drisdell, Z. Wei, M. Gu, K. Amine and M. Shao, Fe–N–C Boosts the Stability of Supported Platinum Nanoparticles for Fuel Cells, *J. Am. Chem. Soc.*, 2022, **144**, 20372–20384.
69 D. Wang, P. Yang, L. Liu, W. Wang and Z. Chen, Atomically dispersed metal-nitrogen-carbon electrocatalysts for oxygen reduction reaction: from synthesis strategies to activity engineering, *Mater. Today Energy*, 2022, **26**, 101017.
70 H. Zhang, Y. Wang, D. Song, L. Wang, Y. Zhang and Y. Wang, Cerium-Based Electrocatalysts for Oxygen Evolution/Reduction Reactions: Progress and Perspectives, *Nanomaterials*, 2023, **13**, 1921.
71 K. Wang, G. Xing, Q. Song and S. Xiao, Micro‐ and Nanostructured Lead Halide

Perovskites: From Materials to Integrations and Devices, *Adv. Mater.*, 2021, **33**, 2000306.
72 Y. Sun, D. Liu, W. Liu, H. Liu, J. Zhao, P. Chen, X. Wang and Y. Cheng, Combination of ZIF-67 derived hollow porous Co9S8 nanocages and MWCNTs for electrochemical hydrogen storage applications, *Int. J. Hydrog. Energy*, 2022, **47**, 37870–37881.
73 J. Xiao, C. Zhao, C. Hu, J. Xi and S. Wang, Pudding-typed cobalt sulfides/nitrogen and sulfur dual-doped hollow carbon spheres as a highly efficient and stable oxygen reduction electrocatalyst, *J. Power Sources*, 2017, **348**, 183–192.
74 M. Alam, K. Ping, M. Danilson, V. Mikli, M. Käärik, J. Leis, J. Aruväli, P. Paiste, M. Rähn, V. Sammelselg, K. Tammeveski, S. Haller, U. I. Kramm, P. Starkov and N. Kongi, Iron Triad-Based Bimetallic M–N–C Nanomaterials as Highly Active Bifunctional Oxygen Electrocatalysts, *ACS Appl. Energy Mater.*, 2024, **7**, 4076–4087.
75 J. Qi, W. Zhang and R. Cao, Porous Materials as Highly Efficient Electrocatalysts for the Oxygen Evolution Reaction, *ChemCatChem*, 2018, **10**, 1206–1220.
76 A. Serov, M. H. Robson, M. Smolnik and P. Atanassov, Tri-metallic transition metal–nitrogen–carbon catalysts derived by sacrificial support method synthesis, *Electrochimica Acta*, 2013, **109**, 433–439.
77 G. Yusibova, J.-M. Assafrei, K. Ping, J. Aruväli, P. Paiste, M. Käärik, J. Leis, H.-M. Piirsoo, A. Tamm, A. Kikas, V. Kisand, P. Starkov and N. Kongi, Bimetallic metal-organic-framework-derived porous cobalt manganese oxide bifunctional oxygen electrocatalyst, *J. Electroanal. Chem.*, 2023, **930**, 117161.
78 C. Wu, X. Zhang, Z. Xia, M. Shu, H. Li, X. Xu, R. Si, A. I. Rykov, J. Wang, S. Yu, S. Wang and G. Sun, Insight into the role of Ni–Fe dual sites in the oxygen evolution reaction based on atomically metal-doped polymeric carbon nitride, *J. Mater. Chem. A*, 2019, **7**, 14001–14010.
79 H. Mao, X. Guo, Y. Fu, H. Yang, Y. Zhang, R. Zhang and X.-M. Song, Enhanced electrolytic oxygen evolution by the synergistic effects of trimetallic FeCoNi boride oxides immobilized on polypyrrole/reduced graphene oxide, *J. Mater. Chem. A*, 2020, **8**, 1821–1828.
80 K. Kisand, A. Sarapuu, A. Kikas, V. Kisand, M. Rähn, A. Treshchalov, M. Käärik, H.-M. Piirsoo, J. Aruväli, P. Paiste, J. Leis, V. Sammelselg, A. Tamm and K. Tammeveski, Bifunctional multi-metallic nitrogen-doped nanocarbon catalysts derived from 5-methylresorcinol, *Electrochem. Commun.*, 2021, **124**, 106932.
81 I. Hussainova, R. Ivanov, S. N. Stamatin, I. V. Anoshkin, E. M. Skou and A. G. Nasibulin, A few-layered graphene on alumina nanofibers for electrochemical energy conversion, *Carbon*, 2015, **88**, 157–164.
82 M. Drozdova, I. Hussainova, D. Pérez-Coll, M. Aghayan, R. Ivanov and M. A. Rodríguez, A novel approach to electroconductive ceramics filled by graphene covered nanofibers, *Mater. Des.*, 2016, **90**, 291–298.
83 S. Ratso, I. Kruusenberg, A. Sarapuu, M. Kook, P. Rauwel, R. Saar, J. Aruväli and K. Tammeveski, Electrocatalysis of oxygen reduction on iron- and cobalt-containing nitrogen-doped carbon nanotubes in acid media, *Electrochimica Acta*, 2016, **218**, 303–310.
84 Q. Pan, Y. Chen, S. Jiang, X. Cui, G. Ma and T. Ma, Insight into the active sites of M–N–C single-atom catalysts for electrochemical CO2 reduction, *EnergyChem*, 2023, **5**, 100114.
85 G. Chen, H. Zhong and X. Feng, Active site engineering of single-atom carbonaceous electrocatalysts for the oxygen reduction reaction, *Chem. Sci.*, 2021, **12**, 15802–15820.
86 X. Wan, Q. Liu, J. Liu, S. Liu, X. Liu, L. Zheng, J. Shang, R. Yu and J. Shui, Iron atom–cluster interactions increase activity and improve durability in Fe–N–C fuel cells, *Nat. Commun.*, 2022, **13**, 2963.
87 H. Zhong, C. Campos-Roldán, Y. Zhao, S. Zhang, Y. Feng and N. Alonso-Vante, Recent Advances of Cobalt-Based Electrocatalysts for Oxygen Electrode Reactions and Hydrogen Evolution Reaction, *Catalysts*, 2018, **8**, 559.

88 Y. Wu, X. Wu, T. Tu, P. Zhang, J. Li, Y. Zhou, L. Huang and S. Sun, Controlled synthesis of FeNx-CoNx dual active sites interfaced with metallic Co nanoparticles as bifunctional oxygen electrocatalysts for rechargeable Zn-air batteries, *Appl. Catal. B Environ.*, 2020, **278**, 119259.
89 L. Osmieri, Transition Metal–Nitrogen–Carbon (M–N–C) Catalysts for Oxygen Reduction Reaction. Insights on Synthesis and Performance in Polymer Electrolyte Fuel Cells, *ChemEngineering*, 2019, **3**, 16.
90 C. Yang, X. Ma, J. Zhou, Y. Zhao, X. Xiang, H. Shang and B. Zhang, Recent advances in metal-organic frameworks-derived carbon-based electrocatalysts for the oxygen reduction reaction, *Int. J. Hydrog. Energy*, 2022, **47**, 21634–21661.
91 S. Macchi, I. Denmark, T. Le, M. Forson, M. Bashiru, A. Jalihal and N. Siraj, Recent Advancements in the Synthesis and Application of Carbon-Based Catalysts in the ORR, *Electrochem*, 2021, **3**, 1–27.
92 C. Singh, S. Mukhopadhyay and I. Hod, Metal–organic framework derived nanomaterials for electrocatalysis: recent developments for CO2 and N2 reduction, *Nano Converg.*, 2021, **8**, 1.
93 S. Liu, Z. Wang, S. Zhou, F. Yu, M. Yu, C. Chiang, W. Zhou, J. Zhao and J. Qiu, Metal–Organic‐Framework‐Derived Hybrid Carbon Nanocages as a Bifunctional Electrocatalyst for Oxygen Reduction and Evolution, *Adv. Mater.*, 2017, **29**, 1700874.
94 R. R. Salunkhe, J. Tang, Y. Kamachi, T. Nakato, J. H. Kim and Y. Yamauchi, Asymmetric Supercapacitors Using 3D Nanoporous Carbon and Cobalt Oxide Electrodes Synthesized from a Single Metal–Organic Framework, *ACS Nano*, 2015, **9**, 6288–6296.
95 B. Y. Xia, Y. Yan, N. Li, H. B. Wu, X. W. Lou and X. Wang, A metal–organic framework-derived bifunctional oxygen electrocatalyst, *Nat. Energy*, 2016, **1**, 15006.
96 L. Ye, G. Chai and Z. Wen, Zn‐MOF‐74 Derived N‐Doped Mesoporous Carbon as pH‐Universal Electrocatalyst for Oxygen Reduction Reaction, *Adv. Funct. Mater.*, 2017, **27**, 1606190.
97 L. Zhang, Z. Su, F. Jiang, L. Yang, J. Qian, Y. Zhou, W. Li and M. Hong, Highly graphitized nitrogen-doped porous carbon nanopolyhedra derived from ZIF-8 nanocrystals as efficient electrocatalysts for oxygen reduction reactions, *Nanoscale*, 2014, **6**, 6590–6602.
98 R. Kumar, M. Mooste, Z. Ahmed, S. Akula, I. Zekker, M. Marandi, M. Käärik, J. Leis, A. Kikas, A. Treshchalov, M. Otsus, J. Aruväli, V. Kisand, A. Tamm and K. Tammeveski, Highly active ZIF-8@CNT composite catalysts as cathode materials for anion exchange membrane fuel cells, *Ind. Chem. Mater.*, 2023, **1**, 526–541.
99 H.-W. Wang, C. Bringans, A. J. R. Hickey, J. A. Windsor, P. A. Kilmartin and A. R. J. Phillips, Cyclic Voltammetry in Biological Samples: A Systematic Review of Methods and Techniques Applicable to Clinical Settings, *Signals*, 2021, **2**, 138–158.
100 V. Di Noto, G. Pagot, E. Negro, K. Vezzù, P. J. Kulesza, I. A. Rutkowska and G. Pace, A formalism to compare electrocatalysts for the oxygen reduction reaction by cyclic voltammetry with the thin-film rotating ring-disk electrode measurements, *Curr. Opin. Electrochem.*, 2021, 100839.
101 J. Rossmeisl, K. D. Jensen, A. S. Petersen, L. Arnarson, A. Bagger and M. Escudero-Escribano, Realistic Cyclic Voltammograms from Ab Initio Simulations in Alkaline and Acidic Electrolytes, *J. Phys. Chem. C*.
102 M. Rafiee, D. J. Abrams, L. Cardinale, Z. Goss, A. Romero-Arenas and S. S. Stahl, Cyclic voltammetry and chronoamperometry: mechanistic tools for organic electrosynthesis, *Chem. Soc. Rev.*, 2024, **53**, 566–585.
103 A. J. Bard and L. R. Faulkner, *Electrochemical methods: fundamentals and applications*, Wiley, New York, 2nd ed., 2001.
104 J. K. Nørskov, T. Bligaard, A. Logadottir, J. R. Kitchin, J. G. Chen, S. Pandelov and

U. Stimming, Trends in the Exchange Current for Hydrogen Evolution, *J. Electrochem. Soc.*, 2005, **152**, J23.
105 N. Talukder, Y. Wang, B. B. Nunna and E. S. Lee, An In-Depth Exploration of the Electrochemical Oxygen Reduction Reaction (ORR) Phenomenon on Carbon-Based Catalysts in Alkaline and Acidic Mediums, *Catalysts*, 2022, **12**, 791.
106 Y. Garsany, O. A. Baturina, K. E. Swider-Lyons and S. S. Kocha, Experimental Methods for Quantifying the Activity of Platinum Electrocatalysts for the Oxygen Reduction Reaction, *Anal. Chem.*, 2010, **82**, 6321–6328.
107 B. Zhu, R. Zou and Q. Xu, Metal–Organic Framework Based Catalysts for Hydrogen Evolution, *Adv. Energy Mater.*, 2018, **8**, 1801193.
108 K. Ping, A. Braschinsky, M. Alam, R. Bhadoria, V. Mikli, A. Mere, J. Aruväli, P. Paiste, S. Vlassov, M. Kook, M. Rähn, V. Sammelselg, K. Tammeveski, N. Kongi and P. Starkov, Fused Hybrid Linkers for Metal–Organic Framework-Derived Bifunctional Oxygen Electrocatalysts, *ACS Appl. Energy Mater.*, 2020, **3**, 152–157.
109 A. Heuer-Jungemann, N. Feliu, I. Bakaimi, M. Hamaly, A. Alkilany, I. Chakraborty, A. Masood, M. F. Casula, A. Kostopoulou, E. Oh, K. Susumu, M. H. Stewart, I. L. Medintz, E. Stratakis, W. J. Parak and A. G. Kanaras, The Role of Ligands in the Chemical Synthesis and Applications of Inorganic Nanoparticles, *Chem. Rev.*, 2019, **119**, 4819–4880.
110 L. Jin, K. Wu, M. Liao, D. Wang, B. Jayaraman, S. G. Peera and C. Liu, Theoretical analysis of single Zn atoms with N/C on graphene promoting oxygen redox in alkaline medium, *Mol. Catal.*, 2024, **553**, 113799.
111 F. Dalton, ECS Classics: Historical Origins of the Rotating Ring-Disk Electrode, *Interface Mag.*, 2016, **25**, 50–59.
112 D. Song, C. Hu, Z. Gao, B. Yang, Q. Li, X. Zhan, X. Tong and J. Tian, Metal–Organic Frameworks (MOFs) Derived Materials Used in Zn–Air Battery, *Materials*, 2022, **15**, 5837.
113 Y. Huang, Y. Chen, M. Xu, A. Ly, A. Gili, E. Murphy, T. Asset, Y. Liu, V. De Andrade, C. U. Segre, A. L. Deriy, F. De Carlo, M. Kunz, A. Gurlo, X. Pan, P. Atanassov and I. V. Zenyuk, Catalysts by pyrolysis: Transforming metal-organic frameworks (MOFs) precursors into metal-nitrogen-carbon (M-N-C) materials, *Mater. Today*, 2023, **69**, 66–78.
114 J. Lilloja, E. Kibena-Põldsepp, A. Sarapuu, M. Käärik, J. Kozlova, P. Paiste, A. Kikas, A. Treshchalov, J. Leis, A. Tamm, V. Kisand, S. Holdcroft and K. Tammeveski, Transition metal and nitrogen-doped mesoporous carbons as cathode catalysts for anion-exchange membrane fuel cells, *Appl. Catal. B Environ.*, 2022, **306**, 121113.
115 X.-G. Wu, R. Wang, F. Ma, X.-L. Liu, D.-L. Jia, H.-C. Yang, Y.-P. Liu, Z.-X. Wang, H.-Z. Zheng, Y.-N. Zhang, J. Hou, J.-J. Huang and S.-L. Peng, FeCo-N encapsuled in nitrogen-doped carbon nanotubes as bifunctional electrocatalysts with a high stability for zinc air batteries, *Rare Met.*, 2023, **42**, 1526–1534.
116 J. Li, M. T. Sougrati, A. Zitolo, J. M. Ablett, I. C. Oğuz, T. Mineva, I. Matanovic, P. Atanassov, Y. Huang, I. Zenyuk, A. Di Cicco, K. Kumar, L. Dubau, F. Maillard, G. Dražić and F. Jaouen, Identification of durable and non-durable FeNx sites in Fe–N–C materials for proton exchange membrane fuel cells, *Nat. Catal.*, 2020, **4**, 10–19.
117 X. Xie, C. He, B. Li, Y. He, D. A. Cullen, E. C. Wegener, A. J. Kropf, U. Martinez, Y. Cheng, M. H. Engelhard, M. E. Bowden, M. Song, T. Lemmon, X. S. Li, Z. Nie, J. Liu, D. J. Myers, P. Zelenay, G. Wang, G. Wu, V. Ramani and Y. Shao, Performance enhancement and degradation mechanism identification of a single-atom Co–N–C catalyst for proton exchange membrane fuel cells, *Nat. Catal.*, 2020, **3**, 1044–1054.

## Acknowledgments

I would like to express my sincere gratitude to my supervisors, Nadežda Kongi and Gulnara Yusibova, for their unwavering support, invaluable guidance, and insightful feedback throughout the entirety of my master's journey. Their expertise and encouragement have been instrumental in shaping the direction and quality of this thesis.

I am immensely thankful to all our research group and my colleagues: Akmal Kosimov, Iuliia Vetik, Vitali Grozovski, Vladislav Ivaništšev, Ivan Tito Wojsiat Boere R C Souza, and Gunel Mammadova. Their collaboration, intellectual discussions, and support have greatly contributed to the success of this project.

Special appreciation goes to my dear friend Juli Mukhadze for providing mental support and assistance with my work. Your encouragement has been invaluable to me.

To all my friends, especially Ayan Bashirova, Ingerid Ismayılova, and Yahya Babashov, who have been miles away but have never ceased to support me throughout this journey, your encouragement has been my guiding light.

My heartfelt gratitude extends to my Science and Technology family for their consistent presence and support, regardless of the circumstances. Your camaraderie has been a pillar of strength.

Lastly, I owe the greatest thanks to my family, Chimnaz Abdullayeva, Rufat Aliyev and Sultan Aliyev, for their belief in me and their steadfast support during the toughest of times. Your love and encouragement have been the driving force behind my achievements.

I would also like to acknowledge the countless individuals whose contributions, whether acknowledged here or not, have played a significant role in shaping my academic journey and the completion of this thesis.

# Appendix

## Non-exclusive licence to reproduce thesis and make thesis public

I, Amina Aliyeva

1. herewith grant the University of Tartu a free permit (non-exclusive licence) to

reproduce, for the purpose of preservation, including for adding to the DSpace digital archives until the expiry of the term of copyright,

"Synthesis of High-Performance FeCo-N-C Oxygen Electrocatalysts via Zn-TAL MOF Metamorphosis",

supervised by Nadežda Kongi and Gulnara Yusibova,

2. I grant the University of Tartu a permit to make the work specified in p. 1 available to the public via the web environment of the University of Tartu, including via the DSpace digital archives, under the Creative Commons licence CC BY NC ND 3.0, which allows, by giving appropriate credit to the author, to reproduce, distribute the work and communicate it to the public, and prohibits the creation of derivative works and any commercial use of the work until the expiry of the term of copyright.

3. I am aware of the fact that the author retains the rights specified in p. 1 and 2.

4. I certify that granting the non-exclusive licence does not infringe other persons' intellectual property rights or rights arising from the personal data protection legislation.

*Amina Aliyeva*

***30/05/2024***